

## Intra-grain variability of hydrogen and trace elements in rutile

Mona Lueder<sup>a,\*</sup>, Jörg Hermann<sup>a</sup>, Renée Tamblyn<sup>a</sup>, Daniela Rubatto<sup>a,b</sup>, Pierre Lanari<sup>a,b</sup>, Thorsten Andreas Markmann<sup>a</sup>

<sup>a</sup> Institute of Geological Sciences, University of Bern, Baltzerstrasse 1+3, CH-3012 Bern, Switzerland

<sup>b</sup> Institute of Earth Sciences, University of Lausanne, Géopolis, Quartier Mouline, 1015 Lausanne, Switzerland

### ARTICLE INFO

Editor: S. Aulbach

#### Keywords:

Fourier transform infrared spectroscopy  
Zr-in-rutile thermometry  
Trace element mapping  
Hydrogen in rutile  
Rutile Nb/Ta

### ABSTRACT

Rutile is a commonly used petrogenetic indicator mineral to determine metamorphic temperatures, ages, host-/source lithologies, geochemical reservoirs, and subduction conditions. However, intra grain variabilities of trace elements in rutile are rarely considered. We performed trace element and hydrogen mapping of rutile to assess zoning and diffusion in natural rutile from various lithologies. Trace element and hydrogen show distinct zoning patterns, with mostly regular zoning in rutile from pegmatites and low-*T* hydrothermal clefts, and typically irregular zoning in rutile from high-*P* veins and metamorphic rocks. Whereas no clear patterns of trace element correlations can be identified, hydrogen, tri-, tetra- and pentavalent cations can show the same zoning patterns within single rutile grains, despite different substitution mechanisms. This indicates that hydrogen and trace element incorporation is externally controlled by availability and diffusivity of hydrogen and trace elements within the rock matrix, as well as rutile growth rates. H<sub>2</sub>O mapping reveals that hydrogen is retained in rutile at temperatures of up to ~650 °C. Coupled substitution of hydrogen with divalent and trivalent cations requires coupled diffusion processes for charge balance if hydrogen is diffusively re-equilibrated. Slow diffusion rates and thus relatively high temperatures for diffusive closure in rutile lead to retention of primary hydrogen and trace element zoning. At high-*T* conditions of >650 °C, diffusive re-equilibration of all trace elements can be observed. Complex zoning patterns of Zr in rutile show that Zr incorporation into rutile is not purely temperature dependent. In this study, Zr-undersaturation can lead to inaccurate Zr-in-rutile temperatures of up to ~35 °C difference from peak formation temperatures within single rutile grains and might be a useful tool to evaluate rutile growth conditions. Niobium and Ta are highly zoned in rutile, leading to extremely variable Nb/Ta ratios within single rutile grains that cannot be reconstructed from single spot analyses. Overall, mapping offers a novel and promising tool to understanding trace element behavior in rutile.

### 1. Introduction

Rutile is one of the most common accessory minerals in high-grade metamorphic rocks and can also occur in eclogite facies quartz-veins, as needles in fissures, and as cm-sized grains in some pegmatites (Meinhold, 2010, and references therein). Rutile geochemistry is largely host-rock dependent and has multiple applications as petrogenetic indicator. Rutile is a main host of high field strength elements (HFSE), such as Nb and Ta, allowing for Nb/Ta ratios to be used to identify geochemical reservoirs (e.g., Foley et al., 2000; Rudnick et al., 2000; Stepanov and Hermann, 2013). Additionally, Nb and Cr contents allow the differentiation of mafic and felsic rutile (Zack et al., 2004b; Meinhold et al., 2008), with negative log(Cr)/log(Nb) ratios and Nb contents above 800 µg/g being diagnostic of felsic rutile. This allows for the

identification of source lithologies of detrital rutile and can be applied to vein-related rutile to identify fluid sources. The chondritic Nb/Ta ratio lies at about 17.5 (McDonough and Sun, 1995), but most geochemical reservoirs and lithologies have been found to display variable sub-chondritic values between 8 and 14 for continental crust (Barth et al., 2000), ~14 for mid ocean ridge basalt (MORB; Münker et al., 2003), ~11–16 for the depleted mantle (DM; Jochum et al., 2000), and ~16 for ocean island basalt (OIB; Pfänder et al., 2007). It has been suggested that fluid-rock interaction processes in rutile-bearing rocks are able to fractionate Nb and Ta to a significant degree (Huang et al., 2012).

Rutile is also used as temperature indicator in igneous and metamorphic rocks. The temperature dependence of Zr incorporation into rutile has first been shown by Zack et al. (2004a), and a pressure dependence has further been shown by Tomkins et al. (2007). The

\* Corresponding author.

E-mail address: [mona.lueder@unibe.ch](mailto:mona.lueder@unibe.ch) (M. Lueder).

<https://doi.org/10.1016/j.chemgeo.2024.122480>

Received 6 August 2024; Received in revised form 30 October 2024; Accepted 2 November 2024

Available online 5 November 2024

0009-2541/© 2024 The Authors. Published by Elsevier B.V. This is an open access article under the CC BY license (<http://creativecommons.org/licenses/by/4.0/>).

thermometer is based on the exchange of Zr, Si, and Ti between rutile, quartz and zircon, and thus requires rutile to be in equilibrium with zircon and quartz within the sample. Rutile can contain significant amounts of U (10s to 100  $\mu\text{g/g}$ ), which allows for the application of U–Pb geochronology (e.g., Mezger et al., 1989; Kooijman et al., 2010; Zack et al., 2011; Schmitt and Zack, 2012; Bracciali et al., 2013; Xia et al., 2013; Zack and Kooijman, 2017; Hou et al., 2020; Jenkins et al., 2023). However, mafic rutile often has rather low U contents (<5  $\mu\text{g/g}$ ), making U–Pb geochronology challenging. Therefore, it may be useful to establish a mapping-based method to identify domains of elevated U in rutile, to improve the success rates of rutile U–Pb geochronology.

The incorporation of trace elements into rutile depends on their ionic charge and ionic radius of the substituted cation (e.g., Meinhold, 2010). The incorporation mechanism is mainly dependent on the ionic charge. Tetravalent cations can be substituted directly for  $\text{Ti}^{4+}$  (e.g.,  $\text{Ti}^{4+} \rightarrow \text{Zr}^{4+}$ ), whereas the incorporation of di-, tri-, penta-, and hexavalent cations requires coupled substitution to maintain charge balance (e.g., Graham et al., 1973; Tollo and Haggerty, 1987; Urban et al., 1992; Rice et al., 1998; Scott, 2005; Carruzzo et al., 2006; Meinhold, 2010). Trivalent cations can be charge balanced by pentavalent cations (e.g.,  $2 \text{Ti}^{4+} \rightarrow \text{Fe}^{3+} + \text{Nb}^{5+}$ ). Similarly, divalent and hexavalent cations can charge balance each other. Alternatively, two pentavalent cations are required for the charge balance of one divalent cation (e.g.,  $3 \text{Ti}^{4+} \rightarrow \text{Mg}^{2+} + 2 \text{Nb}^{5+}$ ) and two trivalent cations can charge balance one hexavalent cation (e.g.,  $3 \text{Ti}^{4+} \rightarrow 2 \text{Fe}^{3+} + \text{W}^{6+}$ ). Di- and trivalent cations can also be charge balanced by the formation of oxygen vacancies (e.g., Bromiley et al., 2004). Two trivalent cations can be substituted for two  $\text{Ti}^{4+}$  cations, if an oxygen vacancy is formed (e.g.,  $\text{Ti}_2^{4+}\text{O}_4 \rightarrow \text{Fe}_2^{3+}\text{O}_3$ ). Similarly, a  $\text{Ti}^{4+}$  cation can be replaced by one divalent cation along side the formation of an oxygen vacancy (e.g.,  $\text{Ti}^{4+}\text{O}_2 \rightarrow \text{Mg}^{2+}\text{O}$ ). Additionally, rutile can incorporate up to several 1000  $\mu\text{g/g}$   $\text{H}_2\text{O}$  as  $\text{H}^+$ -defect linked to di- and trivalent cations, such as  $\text{Ti}^{3+}$ ,  $\text{Fe}^{3+}$ ,  $\text{Al}^{3+}$ ,  $\text{Mg}^{2+}$ ,  $\text{Fe}^{2+}$ , and  $\text{Cr}^{2+}$  (e.g., Johnson et al., 1968; Hammer and Beran, 1991; Zhang et al., 2001; Bromiley and Hilairt, 2005; Lueder et al., 2023). A trivalent cation is substituted for  $\text{Ti}^{4+}$ , creating a charge deficit that can be balanced by the incorporation of  $\text{H}^+$  onto an interstitial site (e.g.,  $\text{Ti}^{4+}\text{O}_2 \rightarrow \text{Fe}^{3+}\text{H}^+\text{O}_2$ ). Fourier transform infrared spectroscopy (FTIR) mapping has been used to show that  $\text{H}_2\text{O}$  contents in rutile can be zoned and it has been suggested that  $\text{H}^+$  zoning is dependent on inhomogeneous incorporation of trace elements to which  $\text{H}^+$  is coupled (Lueder et al., 2024). In order to assess these possible substitution mechanisms, it is necessary to have combined measurements of  $\text{H}_2\text{O}$  and trace elements in rutile and to know their spatial distribution.

In all of the above mentioned applications of rutile geochemistry, intra grain variabilities of trace element contents in rutile are generally not assessed, with homogeneity often being implicitly assumed. However, it has been shown that core-rim zoning of Zr, Nb and Ta in rutile (e.g., Huang et al., 2012; Kooijman et al., 2012; Kohn et al., 2016; Markmann et al., 2024), zoning of Zr related to deformation features (Verberne et al., 2022), and irregular trace element zoning in rutile associated with mineralizations (e.g., Sciuba and Beaudoin, 2021) can occur. Still, systematic studies of intra grain variability of trace elements in rutile are missing.

In this study, we investigate intra grain variabilities of trace elements and  $\text{H}^+$  in rutile in different lithologies. Mapping of rutile was carried out by laser ablation inductively coupled plasma mass-spectrometry (LA-ICP-MS) and Fourier transform infrared spectroscopy (FTIR). The results reveal trace element zoning patterns and compositions that can be used to infer fluid composition and fluid sources during rutile growth. Further, we evaluate implications of Zr zoning for Zr-in-rutile thermometry. We compare Nb–Ta contents and Nb/Ta ratios from LA-ICP-MS maps with extracted spot data, to discuss the potential applicability of Nb-Ta-mapping to investigate Ta fractionation in (fluid rich) pegmatites and metamorphic rocks. Lastly, we assess the correlation between trace elements and  $\text{H}^+$  in rutile and its possible significance

for trace-element coupling in rutile, as well as coupled diffusion of  $\text{H}^+$  with other trace elements and the implications for  $\text{H}^+$  retentivity.

## 2. Materials and methods

### 2.1. Samples

We investigated nine samples, from high-pressure metamorphic conditions, hydrothermal cleft environments, and pegmatites (Table 1). The hydrothermal sample A7653 is an elongated, light brown single rutile grain of  $\sim 2 \times 0.5 \times 0.5$  cm with prominent ilmenite needles from Faulhorn, Swiss Central Alps (Fig. 1a). Sample A5732 is a columnar  $\sim 1$  cm long, dark-brown rutile grain from a pegmatite from Iragna, Swiss Central Alps (Fig. 1b). The second pegmatitic sample SFJ comes from a Brazilian pegmatite with unknown locality, is elongated and  $\sim 2$  cm long, with one pronounced twin, and reddish-brown color (Fig. 1c).

Metamorphic and vein-related samples include rutile from different localities in the European Alps. Two rutile samples from eclogite lenses within micaschist and paragneiss from Monte Mucrone, Sesia Zone, Western Alps were selected. The eclogites have a mineral assemblage of omphacite, garnet, Na-amphibole, and white mica and record peak metamorphic conditions of  $1.8 \pm 0.1$  GPa and  $550 \pm 50$  °C (Regis et al., 2014; Vho et al., 2020). The selected rutile samples M-Q1 (Fig. 1d) and M-E2 (Fig. 1e) are single, dark-brown grains from quartz veins within the host-eclogite lenses with grain sizes of  $\sim 2.5 \times 5$  mm and  $\sim 1.5 \times 2.5$  mm, respectively. Both samples show ilmenite lamellae.

Two metapelitic amphibolite facies samples from Alpe Senevedo Superiore, Val Malenco, Eastern Central Alps were selected. The samples record peak metamorphic conditions of  $1.0 \pm 0.3$  GPa and  $475 \pm 25$  °C (Bissig and Hermann, 1999). Sample AS19–1 has a mineral assemblage of garnet, phengite, and quartz, with quartz occurring both within the matrix and as quartz-layers. Rutile has a reddish-brown color and occurs in the matrix as  $\sim 200$   $\mu\text{m}$  grains and within the quartz-layer as cm-sized grains showing ilmenite exsolution needles (Fig. 1f). Sample AS19–3 contains a mineral assemblage of garnet, phengite, quartz, chlorite, and green amphibole. Phengite, chlorite and amphibole form a pronounced foliation around larger garnet grains. The mapped rutile grain was from within a quartz lens together with other mm-sized rutile grains (Fig. 1g). It has a size of  $\sim 3 \times 2$  mm and contains inclusions of matrix minerals.

Two samples from Pfulwe, Zermatt-Saas-Zone, Western Alps were collected from a metamorphic Fe-Ti-gabbro with peak metamorphic conditions of  $2.1 \pm 3.0$  GPa and 550–600 °C (Bucher et al., 2005). Sample PF18–14 has a matrix assemblage of chloritoid, omphacite, paragonite, strongly resorbed glaucophane, and small amounts of quartz with inclusion-rich garnet phenocrysts that are rimmed by retrograde amphibole. Rutile occurs as pseudomorph after ilmenite in an aggregate of >100 grains of 100–800  $\mu\text{m}$  size (Fig. 1i). Individual rutile grains contain ilmenite needles and often show dark, blueish-brown cores with light brown rims. Sample PF21–02 is a  $\sim 2$  cm sized rutile grain from a quartz vein within the metagabbro (Fig. 1h). It is dark brown in color and has prominent ilmenite exsolutions.

One metapelite sample (VS23) from Val Strona, Ivrea-Zone, Southern Alps, was collected as loose block within a river. The sample records peak metamorphic conditions of  $0.7 \pm 0.1$  GPa and  $900 \pm 50$  °C (Ewing et al., 2013) and has a mineral assemblage of garnet, sillimanite, quartz, and minor plagioclase. Rutile occurs as dark brown grains of  $\sim 30$ –700  $\mu\text{m}$  with pronounced ilmenite rims.

### 2.2. Sample preparation

The rutile vein samples and whole rock samples from Pfulwe (PF18–14) and Alpe Senevedo Superiore (AS19–3) were prepared as double polished thick sections of 100–120  $\mu\text{m}$  thickness, polished with diamond paste to a grade of 3  $\mu\text{m}$ . The vein-related sample from Pfulwe (PF21–02) and the hydrothermal sample (A7653) were prepared as oriented grains. The grains are elongated along their crystallographic c-

**Table 1**

Sample localities, mineral assemblages, lithologies, peak metamorphic *P-T*-conditions, and calculated maximum Zr-in-rutile temperatures ( $T_{[Zr]}$ ). References: [1] Bucher et al. (2005), [2] Bissig and Hermann (1999), [3] Ewing et al. (2013), [4] Regis et al. (2014). Mineral abbreviations after Warr (2021).

Locality		Sample name	Lithology and mineral assemblage		Grain size (mm)	Metamorphic <i>P-T</i>	$T_{[Zr]}$ (°C)	
Western Alps	Monte Mucrone	45°37'48" N 7°56'31" E	M-Q1	Qz-vein in eclogite	Omp, Grt, Amp, Mca	~2.5 × 5	1.8 ± 0.1 GPa, 550 ± 50 °C [4]	557 ± 1
		45°37'48" N 7°56'31" E	M-E2			~1.5 × 2.5		555 ± 3
	Pfulwe	46°00'59" N 7°50'53" E	PF18-14	Fe-Ti-metagabbro	Grt, Omp, Pg, Gln, Cld, Qz, ± Zrc, ± Ap	~0.1–0.8	2.1 ± 0.3 GPa, 575 ± 25 °C [1]	495 ± 5
		46°00'48" N 7°50'23" E	PF21-02	Qz-vein in metagabbro	Qz, Rt	~20 × 7		517 ± 1
	Ivrea	45°55'56" N 8°15'39" E (river sample)	VS23	Metapelite	Grt, Sil, Qz, ± Pl, ± Zrc, ± Rt, ± Ilm	~0.3 × 0.7	0.7 ± 0.1 GPa, 900 ± 50 °C [3]	1090 ± 13
Central Alps	Faulhorn	A7653	Hydrothermal			~20 × 5		495 ± 1
	Iragna	A5732	Pegmatite			~10 × 2	0.7 ± 0.1 GPa, 650 ± 50 °C	592 ± 2
	Alpe Senevedo Superiore	loose block	AS19-1	Qz-lense in amphibolite	Grt, Qz, Mca, Rt, ± Ap, ± Zrc	~3 × 7	1.0 ± 0.3 GPa, 475 ± 25 °C [2]	484 ± 5
		loose block	AS19-3	facies metapelite	Grt, Qz, Mca, Chl, Amp, Rt, ± Ap, ± Zrc	~5 × 20		490 ± 2
	Brazil	(bought at a gem show)	SFJ	Pegmatite			~5 × 5	

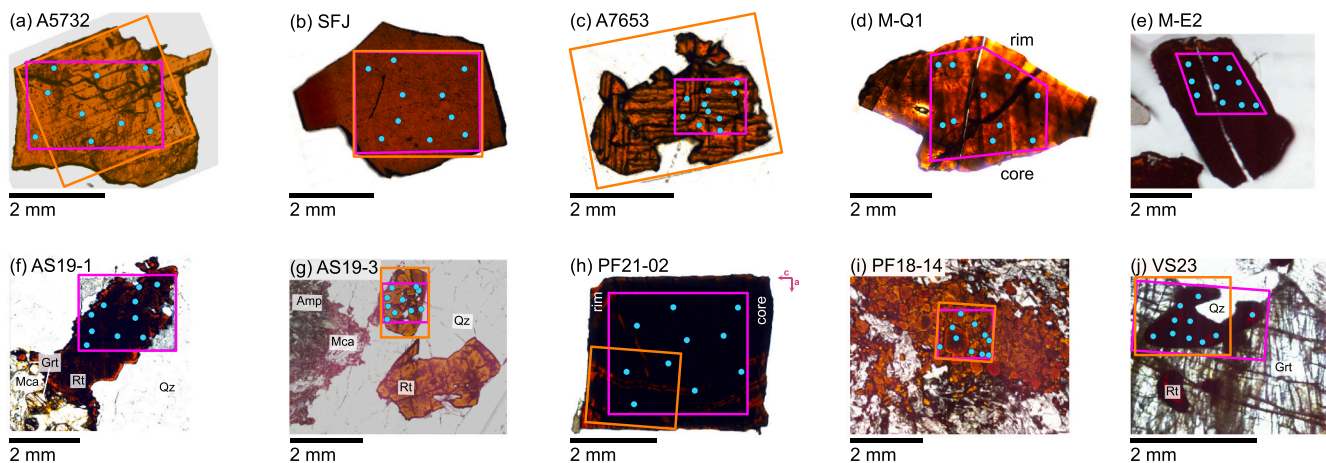


**Fig. 1.** Photomicrographs of double polished rutile grains and thick sections. Pink boxes show areas of LA-ICP-MS trace element maps, orange boxes show FTIR H<sub>2</sub>O mapping areas. Blue circles indicate points for random sampling of Nb and Ta contents. (For interpretation of the references to color in this figure legend, the reader is referred to the web version of this article.)

axis, allowing orientation according to this morphological characteristic. The samples were then cut approximately perpendicular to the crystallographic *c*-axis. Sample PF21-02 was additionally cut parallel to the *c*-axis. The resulting cross-sections, as well as the pegmatitic (A5732, SFJ) and single grain samples from Monte Mucrone (M-E2, M-Q1) were mounted in 2.5 cm-round epoxy mounts and doubly polished to ~100–250 μm thickness. Sample thickness was determined using a vertically mounted mechanical Mitutoyo ID-S112X micrometer with a precision of ±3 μm after the samples were removed from their glass plates and the epoxy was dissolved by leaving them in acetone for ~8–48 h. Samples were re-glued on glass plates for LA-ICP-MS measurements.

### 2.3. FTIR

Transmission Fourier Transform Infrared Spectroscopy (FTIR) was performed at the University of Bern using a Bruker Tensor II spectrometer with a globar infrared source equipped with a Bruker Hyperion 3000 microscope. High-resolution maps were collected using a focal plane array (FPA) detector, composed of 64 × 64 liquid nitrogen cooled

mercury-cadmium-telluride (MCT) elements on a square array. Data were acquired over a wavenumber range of 900–3800 cm<sup>-1</sup> with a resolution of 8 cm<sup>-1</sup>, 64 scans, and a binning of 2, resulting in a spatial resolution of ~5.4 × 5.4 μm. Samples SFJ and AS19-3 were additionally mapped with a resolution of 25 μm following the mapping procedure described in Lueder et al. (2023), due to the large grain size and interference effects in FPA-FTIR measurements. The closed sample chamber was purged with nitrogen gas or dried air during measurements to minimize interference from atmospheric water. Single grain samples were analyzed on CaF<sub>2</sub> plates that are transparent in the measured IR-range. Samples were measured polarized with the electric vector (E) parallel to the crystallographic *a*-axis by rotating the polarisor until the measured spectrum reaches its maximum absorbance (Lueder et al., 2023). Using the OPUS © software provided by Bruker, maps were corrected for interference of atmospheric H<sub>2</sub>O and CO<sub>2</sub>, as well as baseline corrected using the ‘concave rubberband’ method with four iterations and 64 baseline points. Evaluations of FTIR maps was performed using the software SpecXY (Gies et al., 2024). The SpecMaps module allows the exclusion of fractures, mineral inclusions and surrounding phases. Individual trace-element related OH-band positions

were identified by peak deconvolution of fixed width and fixed position Lorentzian peaks in the OH-region. Quantification of total- and trace-element related H<sub>2</sub>O contents is done using a modified Beer-Lambert Law from maximum polarized spectra (Lueder et al., 2023).

#### 2.4. LA-ICP-MS

LA-ICP-MS mapping was performed at the University of Bern using a Resonetics RESOLUTION SE 193 nm excimer laser system equipped with a S-155 large volume constant geometry ablation cell (Laurin Technic, Australia) coupled to an Agilent 7900 quadrupole ICP-MS system. Ablation was performed in an ultra-pure He (0.7 l min<sup>-1</sup>) and N<sub>2</sub> (0.003 l min<sup>-1</sup>) mix with Ar (0.86 l min<sup>-1</sup>) immediately after the ablation cell. A surface energy density on the sample of 7 J/cm<sup>2</sup> and a laser repetition rate of 10 Hz were used. For this, line scans with a scan speed of ~2/3 of the spot size per second was used, to generate overlapping spots, and thus a high spatial resolution (Markmann et al., 2024). Spot sizes of 12–38 μm were chosen, depending on the size of the map area, resulting in a special resolution of ~20 μm. A suite of 26 elements was measured. Primary- (SRM-NIST610, Jochum et al., 2011) and secondary standard (SRM-NIST612, Jochum et al., 2011) were measured approximately

every 15–25 min. Data reduction was performed using the software *XMapTools* (Lanari and Piccoli, 2020; Markmann et al., 2024). A peak function was fitted to the standard measurements to correct for instrument drift, and backgrounds were subtracted from all measurements. All samples were quantified using a fixed value of 59.94 wt% Ti. To correlate H<sub>2</sub>O- and trace-element maps, H<sub>2</sub>O maps were exported from *SpecXY* and superimposed on LA-ICP-MS trace-element maps using the *StackMaps* module in *XMapTools* 3.4.1 (Reynes et al., 2020).

### 3. Results

All investigated rutile grains show trace element zoning. Zoned trace elements and zoning patterns vary strongly between samples and geological settings. Trace elements that show zoning in this study are: Al, Sc, V, Cr, Fe, Zr, Nb, Mo, Sn, Sb, Ta, W, and U. Selected, representative trace element maps are shown in Figs. 2, 3, 4 and 5; all additional trace element maps can be found in Supplementary material A. Additionally, all analyzed samples are inhomogeneous in both total- and trace-element related H<sub>2</sub>O contents, with the exception of sample M-E2 which shows homogenous H<sub>2</sub>O contents.

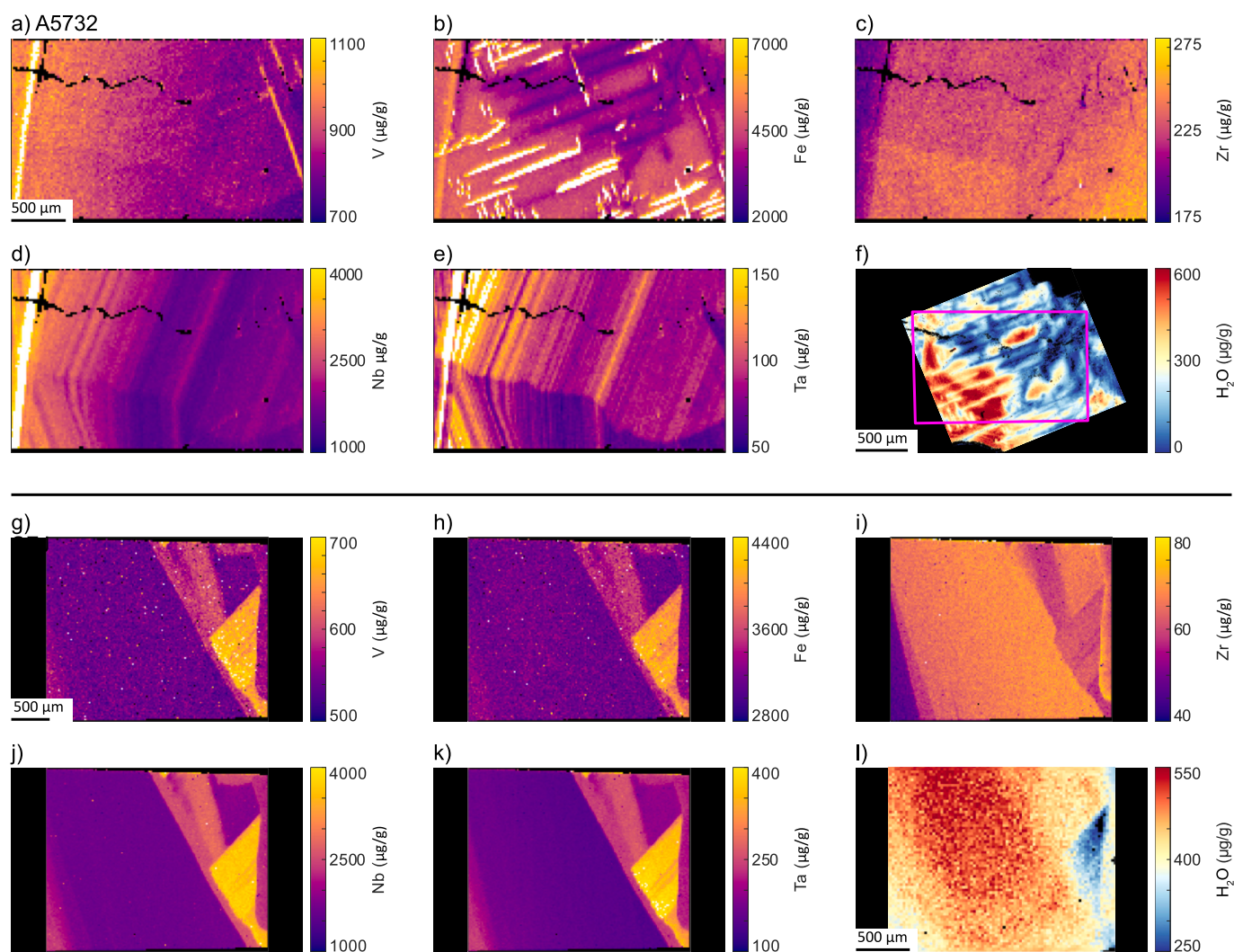


**Fig. 2.** Selected trace element and H<sub>2</sub>O maps of pegmatitic samples A5732 (a-f) and SFJ (g-l) for V (a, g), Fe (b, h), Zr (c, i), Nb (d, j), Ta (e, k), and H<sub>2</sub>O (f, l). Total H<sub>2</sub>O maps are calculated from individual trace element related H<sub>2</sub>O maps from quantification of deconvolution results. Map areas shown in Fig. 1a and b. The pink rectangle in (f) shows the location of the trace element map of sample A5732. Trace element and H<sub>2</sub>O map locations for sample SFJ are nearly identical. Additional trace element maps can be found in Supplementary Material A1 and A2. Trace element related H<sub>2</sub>O maps can be found in supplementary material B1 and B2. White areas in a)-e) and g)-k) are above the maximum value of the color bar. (For interpretation of the references to color in this figure legend, the reader is referred to the web version of this article.)

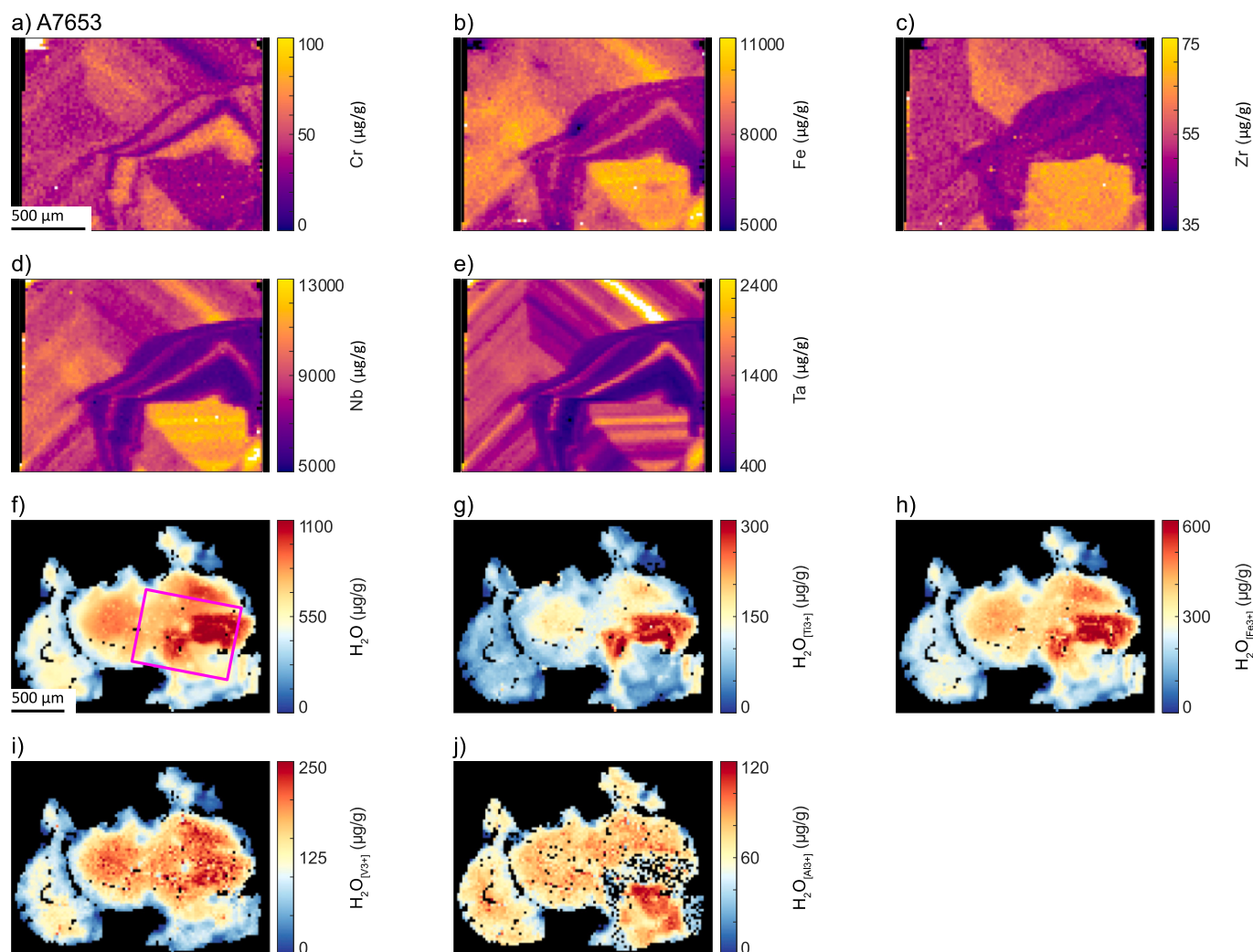


**Fig. 3.** Selected trace element maps and total- and trace element related H<sub>2</sub>O maps for hydrothermal sample A7653. Trace element maps for Cr (a), Fe (b), Zr (c), Nb (d), and Ta (e). Total H<sub>2</sub>O contents (f) are calculated from deconvolution results for H<sup>+</sup> related to Ti<sup>3+</sup> (g), Fe<sup>3+</sup> (h), V<sup>3+</sup> (i), and Al<sup>3+</sup> (j). Map areas are shown in Fig. 1c. The trace element map area is shown as pink square in (f). Additional trace element maps can be found in Supplementary Material A3. White areas in a-e) are above the maximum value of the color bar. (For interpretation of the references to color in this figure legend, the reader is referred to the web version of this article.)

### 3.1. Pegmatitic rutile

Trace elements in sample A5732 can be divided into two groups based on zoning patterns (Supplementary material A1). (i) Fe (Fig. 2b) and Al show two regions of relatively homogeneous trace-element contents. Additionally, needle-like striations can be seen that are either high in Fe and low in Al or low in Fe and high in Al. (ii) Vanadium (Fig. 2a), Zr (Fig. 2c), Sc, Cr, Mo, and Sn show a slight compositional gradient, with Sc and V being inversely correlated to Cr, Zr, Mo, and Sn. Niobium (Fig. 2d), Ta (Fig. 2e), W, and U also show a general gradient, with additionally oscillatory (20–50 µm scale) and/or sector zoning. This is most pronounced for Ta and least pronounced for W. Niobium, Ta, and W also show sector zoning whereby the element composition changes across sectors, but the oscillatory zoning continues across the sector boundary.

Sample A5732 is zoned in total (Fig. 2f) and trace-element related (Supplementary material B1) H<sub>2</sub>O contents. The H<sub>2</sub>O zoning does not show the sector zoning or oscillatory zoning observed in most trace elements. Instead, H<sub>2</sub>O contents show some of the features observed for Al and Fe. The Ti<sup>3+</sup>- and Fe<sup>3+</sup>-related H<sub>2</sub>O contents are approximately the same, whereas Al<sup>3+</sup>-related H<sub>2</sub>O contents are half compared to the other trace-element related H<sub>2</sub>O contents. The H<sub>2</sub>O distribution also displays needle-like features, which however do not correspond to those of the

trace elements.

Sample SFJ shows prominent sector-like zoning in all measured trace elements (Supplementary material A2). Five main sectors can be identified with generally sharp boundaries between sectors and clear variations in trace element contents (e.g. V, Fe, Zr, Nb and Ta in Fig. 2g-k).

Sample SFJ shows sector zoning in Ti<sup>3+</sup>-related, Fe<sup>3+</sup>-related (Supplementary material B2), and total H<sub>2</sub>O (Fig. 2l) content similar to the trace elements. Total H<sub>2</sub>O contents are fairly homogeneous within the individual sectors at ~250–550 µg/g. Trace-element related H<sub>2</sub>O contents follow the same pattern with ~75–325 µg/g Ti<sup>3+</sup>-related H<sub>2</sub>O and ~140–300 µg/g Fe<sup>3+</sup>-related H<sub>2</sub>O. Thus, Fe<sup>3+</sup>-related H<sub>2</sub>O contents vary more strongly between sectors than Ti<sup>3+</sup>-related H<sub>2</sub>O. The mapping areas for trace elements and H<sub>2</sub>O contents of sample SFJ are very similar (Fig. 1b, 2g-l) and the observed sectors are visually comparable.

### 3.2. Hydrothermal cleft rutile

In sample A7653, two different types of zoning are observed on different scales. All trace elements show sector zoning at scale of 100 s of µm (Supplementary material A3). Within each sector, all trace elements show an additional oscillatory zoning where each oscillation is approximately 20–100 µm wide. On the oscillatory zoning scale, two groups of trace elements can be seen. Group I is comprised of Cr

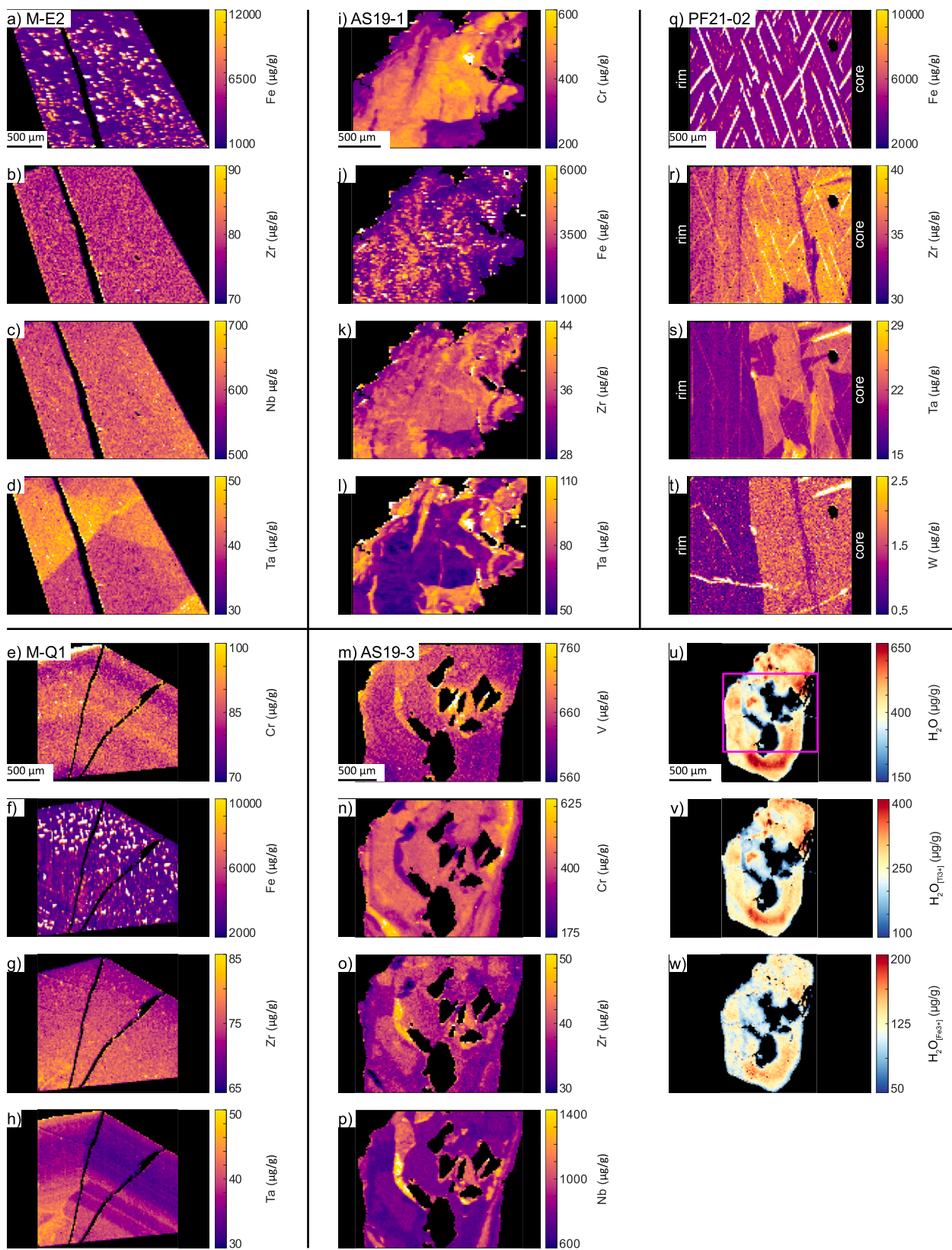


**Fig. 4.** Selected trace element maps for vein related samples M-E2 (a-d), M-Q1 (e-h), AS19-1 (i-l), AS19-3 (m-p), and PF21-02 (q-t), as well as total and trace element related H<sub>2</sub>O maps for sample AS19-3 (t-v). Total H<sub>2</sub>O contents (u) are calculated from deconvolution results for H<sup>+</sup> related to Ti<sup>3+</sup> (v) and Fe<sup>3+</sup> (w). Map areas show in Fig. 1d-h. The pink rectangle in (u) shows the trace element mapping area for sample AS19-3. Additional trace element maps can be found in Supplementary Material A4, A5, A6, A7 and A8. White areas in a-t) are above the maximum value of the color bar. (For interpretation of the references to color in this figure legend, the reader is referred to the web version of this article.)

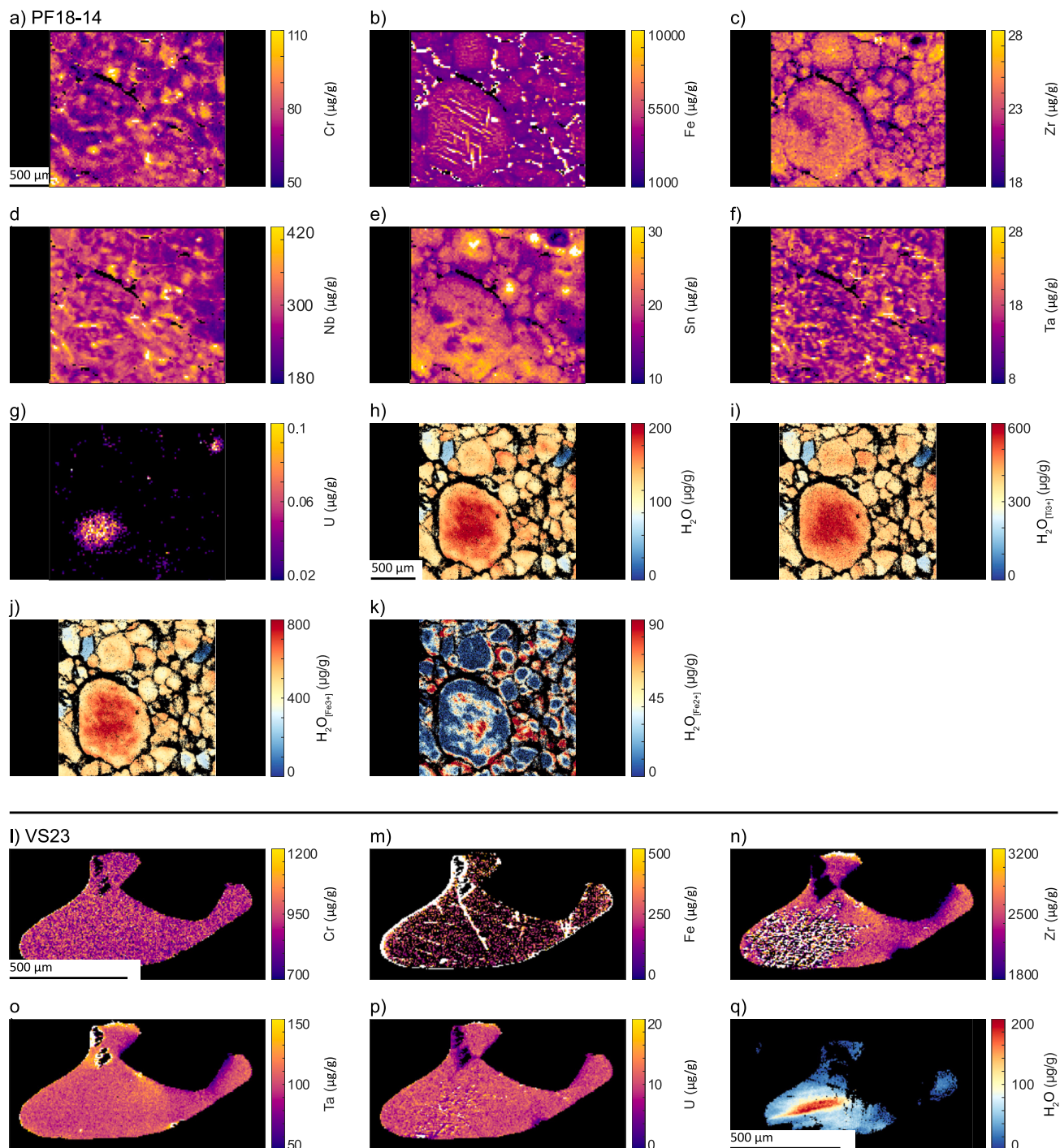


**Fig. 5.** Selected trace element maps and total- and trace element related H<sub>2</sub>O maps for metamorphic samples PF18-14 (a-k) and VS23 (l-q). Trace element maps for sample PF18-14 for Cr (a), Fe (b), Zr (c), Nb (d), Sn (e), Ta (f), U (g); for VS23 for Cr (l), Fe (m), Zr (n), Ta (o), and U (p). Total H<sub>2</sub>O contents (h, q) are calculated from deconvolution results for H<sup>+</sup>. H<sup>+</sup> contents related to Ti<sup>3+</sup> (i), Fe<sup>3+</sup> (j), and Fe<sup>2+</sup> (k) are shown for sample PF18-14. Map areas show in Fig. 1i and j. Trace element and H<sub>2</sub>O maps of both samples are nearly identical. Additional trace element maps can be found in Supplementary Material A9 and A10. White areas in a-g) and l-p) are above the maximum value of the color bar.

(Fig. 3a), Zr (Fig. 3c), Sc, Sn, and U, which are correlated to each other. Group II is comprised of Fe (Fig. 3b), Nb (Fig. 3d), Ta (Fig. 3e), Al, V and Sb. The two groups are anti-correlated to each other.

The hydrothermal cleft sample A7653 also shows sector zoning similar to that observed for the trace elements. Total H<sub>2</sub>O contents vary between ~50–1100 µg/g (Fig. 3f). Zoning for Ti<sup>3+</sup>- and Fe<sup>3+</sup>-related H<sub>2</sub>O (Fig. 3g, h) follows the same pattern as the total H<sub>2</sub>O content with Ti<sup>3+</sup>-related H<sub>2</sub>O of ~20–300 µg/g and Fe<sup>3+</sup>-related H<sub>2</sub>O of ~50–600 µg/g. Generally, Fe<sup>3+</sup>-related H<sub>2</sub>O contents are approximately twice as

high as Ti<sup>3+</sup>-related H<sub>2</sub>O contents. The Al<sup>3+</sup>-related H<sub>2</sub>O content varies between ~0–120 µg/g and is anti-correlated with Ti<sup>3+</sup>- and Fe<sup>3+</sup>-related H<sub>2</sub>O contents (Fig. 3j). The V<sup>3+</sup>-related H<sub>2</sub>O content does not show sector zoning (Fig. 3i), but a general core-rim zoning with ~250 µg/g within the core and decreasing H<sub>2</sub>O content towards the rim at <50 µg/g H<sub>2</sub>O.

### 3.3. Vein-related rutile in metamorphic rocks

Sample M-Q1 shows a patchy texture of high Fe (Fig. 4f) and Al contents towards the rim. Zirconium (Fig. 4g), Ta (Fig. 4h), Sc, Nb and Sb decrease from core to rim, whereas V content increases towards the rim. Mo, Sn and U are homogeneous (Supplementary material A4). Niobium and Ta show oscillatory zoning with a general increase towards the rim. Chromium (Fig. 4e) also shows oscillatory zoning but with no increasing nor decreasing trends from core to rim.

Sample M-E2 is homogeneous in all trace elements but Ta (e.g., Zr Fig. 4b, Nb, Fig. 4c; Supplementary material A5). Ta shows pronounced sector zoning with internally homogeneous sectors of  $\sim 35$   $\mu\text{g/g}$ ,  $\sim 45$   $\mu\text{g/g}$ , and  $\sim 50$   $\mu\text{g/g}$  Ta (Fig. 4d). A patchy texture with areas of high Fe (4a) and Al contents is also observed.

The rutile grain in sample AS19-1 is characterized by an anhedral shape with irregular contours and embayments. It is mostly homogeneous in Al, Mo, Sb, and U (Supplementary material A6), whereas all other trace elements show clear differences between the core and the irregular and patchy zoned rim. Core and rim zones are not concentric and multiple finger-like features can be observed going from the rim-zone into the core-zone. Iron (Fig. 4j), Zr (Fig. 4k), and Sn are higher in the core than at the rim, whereas Cr (Fig. 4i), Ta (Fig. 4l) V, and Nb are higher at the rim. The boundary between core and rim are sharp in Sc, Cr, Zr, Nb, and Ta, and less pronounced in V, Fe, and Sn.

Trace element zoning in rutile from sample AS19-3 is complex (Supplementary material A7). Aluminum, Fe, Mo, Sb, and U are relatively homogeneous, with some needle-like features with very high Fe contents  $>10,000$   $\mu\text{g/g}$ , related to ilmenite exsolutions. Zirconium (Fig. 4o), Nb (Fig. 4p) and Ta show correlating growth zones with generally higher contents in the grain center and relatively lower contents towards the mantle and rim. Niobium and Ta show one mantle zone with highest contents, whereas Zr significantly decreases within that zone before increasing again in the outer most rim. Chromium (Fig. 4n) and Sn show oscillatory zoning on a scale of  $\sim 50$ – $100$   $\mu\text{m}$ , with a general anti-correlation between Cr and Sn. Vanadium (Fig. 4m) shows some of the zones observed for Cr, Zr, Nb (Fig. 4p), and Ta, which are, however, not as sharply defined. Sample AS19-3 has complex zoning in total- and trace element dependent H<sub>2</sub>O content, which does not follow the zoning of most trace elements but is broader and more patchy. Generally, different growth zones can be observed (Fig. 4u), with low total H<sub>2</sub>O contents of  $\sim 150$ – $250$   $\mu\text{g/g}$  and high H<sub>2</sub>O contents of  $\sim 500$ – $650$   $\mu\text{g/g}$ . This zoning pattern is similar to the zoning observed for Cr. It can also be seen that H<sub>2</sub>O contents increase in the mantle, before decreasing towards the outermost rim. In the inner mantle, close to an inclusion of white mica, total H<sub>2</sub>O contents are  $\sim 400$   $\mu\text{g/g}$ . They increase towards the outer mantle at  $\sim 650$   $\mu\text{g/g}$  and decrease again to  $\sim 350$   $\mu\text{g/g}$  at the rim. The Ti<sup>3+</sup>- and Fe<sup>3+</sup>-related H<sub>2</sub>O contents follow the same trend as the total H<sub>2</sub>O content (Fig. 4v, w) with lower Ti<sup>3+</sup>- and Fe<sup>3+</sup>-related H<sub>2</sub>O in the center than towards the rim and the highest H<sub>2</sub>O content being related to the Ti<sup>3+</sup>-defect.

Sample PF21-02 shows a general core-rim zoning parallel to the crystallographic c-axis (Supplementary material A8). Iron (Fig. 4q) and V are homogeneous; Sc, Cr, and U increase towards the rim; Zr (Fig. 4r), Ta (Fig. 4s), W (Fig. 4t), Al, Nb, Mo, Sn and Sb decrease towards the rim. Chromium, Nb, Ta and W show a sharp boundary between low and high contents, whereas Mo, Sn, and Sb show a less clear boundary, and Al, Sc, Zr and U show a rather continuous gradient. One vein-like feature of low Zr, Sn and W contents within the core zone can be observed. Niobium and Ta show an additional patchy zoning within the core zone. Needle-like features with high Fe and V contents are related to ilmenite exsolutions: the needles show clear preferred orientations, with two groups of needles oriented  $\sim 60^\circ$  towards each other and  $\sim 60^\circ$  off the crystallographic c-axis.

### 3.4. Metamorphic rutile

Trace elements in the rutile aggregate of sample PF18-14 (eclogitic Fe-Ti-metagabbro) can be classified into three groups with different zoning patterns (Supplementary material A9). (i) Chromium (Fig. 5a), Nb (Fig. 5d), and Ta (Fig. 5f) show patchy, irregular zoning with no apparent correlations. Zirconium (Fig. 5c), Sn (Fig. 5e), and Mo show areas of low contents in the center of one large grain and higher content towards the rim. Small grains have high Zr, Mo, and Sn contents in the core and lower contents towards the rims. Molybdenum and Sn strongly correlate, whereas Zr is less strongly correlated. Uranium (Fig. 5g) contents are generally low ( $<0.1$   $\mu\text{g/g}$ ), though a clear core-rim zonation in a large rutile grain is visible, with U-contents in the core being about 1 order of magnitude higher than in the rim. Vanadium also shows a general core-rim zoning in one large rutile grain, however, V zoning is much smoother compared to other trace elements and partially even flattened out across grain boundaries. Iron (Fig. 5b) and Al are relatively homogeneous, with some Fe-rich needles, related to ilmenite exsolutions. Total- (Fig. 5h), Ti<sup>3+</sup>- (Fig. 5i), Fe<sup>3+</sup>- (Fig. 5j), and Fe<sup>2+</sup>-related (Fig. 5k) H<sub>2</sub>O contents of the rutile aggregate in sample PF18-14 generally show core-rim zoning that resemble that of the trace elements. The highest H<sub>2</sub>O contents is observed in the core of one large grain at  $\sim 1400$   $\mu\text{g/g}$ . H<sub>2</sub>O contents decrease towards the rim to  $\sim 800$   $\mu\text{g/g}$ . The high H<sub>2</sub>O content correlates to a darker, ilmenite inclusion-rich area seen in the photomicrograph (Fig. 1i). Smaller grains mainly show higher H<sub>2</sub>O contents at the rim. One grain with very low trace-element contents also has very low H<sub>2</sub>O contents. The Ti<sup>3+</sup>- and Fe<sup>3+</sup>-related H<sub>2</sub>O contents show the same zoning pattern observed for the total H<sub>2</sub>O content (Fig. 4h, i), with  $\sim 600$   $\mu\text{g/g}$  H<sub>2</sub>O<sub>[Ti3+]</sub> and  $\sim 800$   $\mu\text{g/g}$   $\sim$  H<sub>2</sub>O<sub>[Fe3+]</sub> in the core, and  $\sim 400$   $\mu\text{g/g}$  H<sub>2</sub>O<sub>[Ti3+]</sub> and  $\sim 400$   $\mu\text{g/g}$   $\sim$  H<sub>2</sub>O<sub>[Fe3+]</sub> at the rim. The Fe<sup>2+</sup>-related H<sub>2</sub>O content also shows a similar pattern with  $\sim 90$   $\mu\text{g/g}$  in the core and  $< 20$   $\mu\text{g/g}$  towards the rim. However, a pronounced increase in Fe<sup>2+</sup>-related H<sub>2</sub>O to  $\sim 90$   $\mu\text{g/g}$  can be seen in the outer most  $\sim 20$   $\mu\text{m}$  of most grains.

Sample VS23 (granulite-facies metapelite) shows no trace-element zoning in most elements (Supplementary material A10). Iron (Fig. 5m), Al, and Sc show needle like features and increase at the very rim. Zirconium (Fig. 5n) and U (Fig. 5p) are mainly unzoned, however, in one part of the grain (area of  $\sim 500 \times 250$   $\mu\text{m}$ ) an aggregation of Zr- and U-rich needle-like features can be seen, likely representing sub-microscopic zircon exsolutions, as described by Ewing et al. (2013) and Pape et al. (2016) for the sample locality, as well as Meyer et al. (2011) for granulite facies rutile from the Epupa Complex, NW Namibia. All other trace elements do not show zoning (e.g., Cr, Fig. 5l, Ta, Fig. 5o), with minor patchy areas seen in Nb and Ta. Granulite-facies sample VS23 shows a pronounced core-rim zonation of total H<sub>2</sub>O contents (Fig. 5q) that is distinct from the homogeneous distribution of trace elements. The highest H<sub>2</sub>O contents of  $\sim 180$   $\mu\text{g/g}$  are seen in the core, forming an area elongated approximately perpendicular ( $\sim 75^\circ$ ) to the crystallographic a-axis. Parallel to the a-axis, H<sub>2</sub>O contents continuously decrease towards  $\sim 30$   $\mu\text{g/g}$  at the rim, whereas the decrease perpendicular to the a-axis is much less pronounced.

## 4. Discussion

All analyzed samples show trace-element and H<sub>2</sub>O zoning with different zoning patterns that can be classified into regular zoning and irregular zoning. Correlating H<sub>2</sub>O and trace-element zoning can be used to quantify trace-element coupling and charge balance in rutile and can give information on (coupled) diffusion in rutile. Rutile is commonly zoned in Cr, Zr, Nb and Ta, which makes rutile trace element maps a potentially interesting tool for the application of rutile as petrogenetic indicator through (i) classification of host/source lithologies using Cr and Nb contents, (ii) Zr-in-rutile thermometry, and (iii) identification of source reservoirs from Nb/Ta ratios.

#### 4.1. Trace element zoning in rutile

Trace element contents can be quite variable between different samples. Aluminum, Fe and V contents are comparable between all samples (100–800 µg/g Al, 2000–5000 µg/g Fe, 400–900 µg/g V), with the exception of higher Fe contents in hydrothermal sample A7653 and higher V contents in the high-*T* metamorphic sample VS23. Chromium contents are variable between 40 and 900 µg/g, independent of sample lithology. Zirconium contents are generally low (20–80 µg/g), with elevated Zr contents observed in pegmatitic sample A5732 (230 ± 13 µg/g) and significantly higher Zr contents in the high-*T* metamorphic sample VS23 (2425 ± 1800 µg/g). Niobium, Ta, Sc, Sn and U contents vary depending on sample lithology. Niobium and Ta contents are elevated in felsic rutile (pegmatitic, hydrothermal, metapelitic, high-*P* veins in metapelites, 1400–9000 µg/g Nb, 70–200 µg/g Ta) compared to mafic rutile (metagabbro, high-*P* veins in mafic rocks, 250–850 µg/g Nb, 15–40 µg/g Ta), with one order of magnitude higher Nb and Ta contents in the hydrothermal cleft sample A7653 (8680 ± 1620 µg/g Nb, 1190 ± 380 µg/g Ta). Similarly, U contents are generally low in mafic rutile and vein-related rutile (< 0.1–2.5 µg/g) and higher in the pegmatitic and hydrothermal rutile samples, as well as the metapelitic sample VS23 (8–25 µg/g). Scandium and Sn contents are generally low in vein-related and metamorphic rutile samples (1–5 µg/g Sc, 20–35 µg/g Sn) and higher in hydrothermal and pegmatitic rutile (10–30 µg/g Sc, 100–750 µg/g Sn). Pegmatitic rutile shows relatively higher Sc contents (20–30 µg/g), whereas hydrothermal rutile has comparably higher Sn contents (650 ± 110 µg/g).

All samples show distinctly different zoning patterns, and no clear patterns or consistent trace element behavior can be observed. Multiple trace elements can be correlated or un-correlated depending on the sample. Although no general correlation trends can be identified, there are groups of trace elements that are more likely to be correlated: i) Al and Fe, ii) Sc, Zr, Nb, and Ta, iii) Cr anti-correlates with (ii), and V, Sn, and W can be correlated or anti-correlated with (ii). Additionally, it can be observed for this sample set that samples from pegmatites and hydrothermal conditions show more regular zoning, whereas metamorphic rutile from both high-*P* metamorphic veins and as accessory phase in the matrix, are more likely to show irregular zoning (Table 2).

We observe two different types of regular zoning: sector zoning and oscillatory zoning. Oscillatory zoning is characterized by continuous variations of higher and lower trace element contents with sharp boundaries between different oscillations. Oscillatory zoning in rutile has been explained by different factors (Carocci et al., 2019, and references therein) such as the changing composition of the melt or the hydrothermal fluid. Alternatively, a faster rutile growth rate than diffusion rates of trace elements in the fluid/melt, can result in the formation of a boundary layer at the crystal interface, even when the bulk external fluid/melt composition is invariable (Carocci et al., 2019). Sector zoning is marked by different trace element contents in different growth faces, which leads to sharp, often non-straight boundaries between different sectors. Sector zoning is a growth-related feature, commonly observed in magmatic minerals (e.g., pyroxene: Nakamura, 1973), and is common in ore-related hydrothermal rutile (e.g., Rice et al., 1998; Carocci et al., 2019). Different mechanisms have been proposed for the formation/preservation of sector zoning, all relying on either different growth rates, growth mechanisms, atomic configurations, or diffusion rates depending on the crystal faces (e.g., Rice et al., 1998, and references therein). Oscillatory zoning and sector zoning can occur within the same grain superimposing oscillatory zoning within each individual sector, as can be observed for pegmatitic sample A5732 and hydrothermal cleft sample A7653. Additionally, minor sector- and oscillatory zoning can be observed in the vein-related rutile M-Q1.

Irregular zoning is mostly observed in veins and metamorphic samples. Vein rutile AS19–3 and PF21–02, as well as pegmatitic rutile SFJ shows “angular zoning” with sharp, relatively straight boundaries between zones. Unlike sector zoning however, these boundaries are very

**Table 2**

Classification of observed trace element zoning as regular (sector or oscillatory) zoning vs. irregular (angular or cloudy) zoning. (\*) – minor degree of zoning observed. See text for definitions of zoning.

Sample	Lithology	Regular zoning		Irregular zoning	
		Sector zoning	Oscillatory zoning	Angular	Cloudy
A5732	Pegmatite	V*, Zr*, Nb, Sn*, Ta, W, U*	Nb, Ta, W*, U		Al, Fe
SFJ	Pegmatite			Al, Sc, V, Cr, Fe, Zr, Nb, Sn, Sb, Ta, U	
A7653	Hydrothermal cleft	Al, Sc, V, Cr, Fe, Zr, Nb, Sn, Sb, Ta, U	Sc*, V*, Cr, Fe*, Zr*, Nb, Sn, Ta, U*		
M-Q1	Vein-related	Nb*, Ta	Cr*, Nb*, Ta		Al, Fe
M-E2	Vein-related			Ta	Al, Fe
AS19–1	Metamorphic vein-related				Al*, Sc, V*, Cr, Fe*, Zr, Nb, Sn, Ta
AS19–3	Vein-related			V*, Cr, Zr, Nb, Sn, Ta	V*
PF21–02	Vein-related			Cr, Zr*, Nb, Sn, Ta, W	
PF18–14	Metamorphic				V*, Cr, Zr, Nb, Mo, Sn, Sb*, Ta, U*
VS23	Metamorphic				Zircon exsolutions

linear, which can be best seen in comparison to Ta zoning in sample M-E2 (Fig. 4d) and sample A5732 (Fig. 2e). This type of zoning has previously been reported by Sciuba and Beaudoin (2021) for rutile from sediment-hosted orogenic gold deposits. Irregular zoning with soft or curved boundaries of zones, i.e., “cloudy zoning”, can be observed in vein-related sample AS19–1 and metamorphic sample PF18–14. In the vein-related sample AS19–1 a sharp difference in Sc, Cr, Zr, Nb, Sn, and Ta between core and rim can be observed. The boundary between core and rim is irregular and indicates resorption of the core before the rim growth suggesting a two-stage growth process. The finger-like features going from the rim into the core could either be resorption features or fracture fillings. Similar zoning in major or trace elements (e.g. Pollok et al., 2008; Ague and Axler, 2016; Giuntoli et al., 2017; Rubatto et al., 2020) have been observed in metamorphic garnet and attributed to replacement along fractures. Metamorphic sample PF18–14 shows a particular type of cloudy zoning in Cr, Nb, and Ta. As this sample is a Fe-Ti-metagabbro, it is likely that rutile formed as a pseudomorph on a pre-existing ilmenite. Cloudy zoning in zircon has been attributed to growth over a heterogeneous matrix or recrystallization processes (e.g., Corfu et al., 2003, and references therein). Thus, it is plausible that cloudy zoning in rutile would be related to recrystallization in the form of regrowth at sub-solidus conditions during pseudomorphism of rutile after ilmenite. The diffusion-limited uptake of slow-diffusing elements has been described in subsolidus conditions in garnet (Skora et al., 2015). We propose that slow diffusing tetravalent cations (e.g., Zr, Mo, Sn; Dohmen et al., 2019) might mimic the zoning of original ilmenite grains, whereas faster diffusing pentavalent (e.g., Nb, Ta, V; Marschall et al., 2013; Dohmen et al., 2019) and trivalent cations (e.g., Cr) were able to partially re-equilibrate.

As rutile has a very simple composition and with that crystallo-

graphic structure, only one site is available for trace element substitution. However, differently charged cations require different substitution mechanisms. Tetravalent cations (e.g., Zr,  $V^{4+}$ , Hf,  $W^{4+}$ , Sn) can be directly substituted for  $Ti^{4+}$ , whereas tri- and pentavalent cations require coupled substitution for charge balance, e.g.  $2Ti^{4+} \rightarrow Fe^{3+} + Nb^{5+}$ . It can be observed that tri-, tetra- and pentavalent cations can show the same zoning behavior within one rutile grain, with Cr, Zr, Nb and Ta having similar zoning patterns in samples SFJ, A7653, AS19-1, AS19-3, PF21-02 and PF18-14. Additionally, cations with the same charge have different zoning patterns in some rutile. The pentavalent cations Nb and Ta show different zoning behavior in sample M-E2, and the trivalent cations Cr, Al and Fe show different behavior in most samples. Thus, we conclude that zoning is neither controlled by substitution onto different sites, nor by different diffusion mechanisms, nor by

different charge. Consequently, trace element zoning must be externally controlled by diffusivity and availability of trace elements in the matrix, e.g., matrix diffusion, rutile forming reactions, fluid chemistry and saturation, and by rutile growth rates.

The high- $T$  metamorphic sample VS23 is the only sample not showing trace element zoning, suggesting diffusive re-equilibration of all analyzed trace elements at high- $T$  conditions (800–900 °C, see below Zr-in-rutile section). However, the presence of zircon exsolution needles in only one area of the grain might suggest original zoning of trace elements before retrograde re-equilibration.

#### 4.2. $H_2O$ zoning

In all investigated samples  $H_2O$  zoning is observed, with zoning

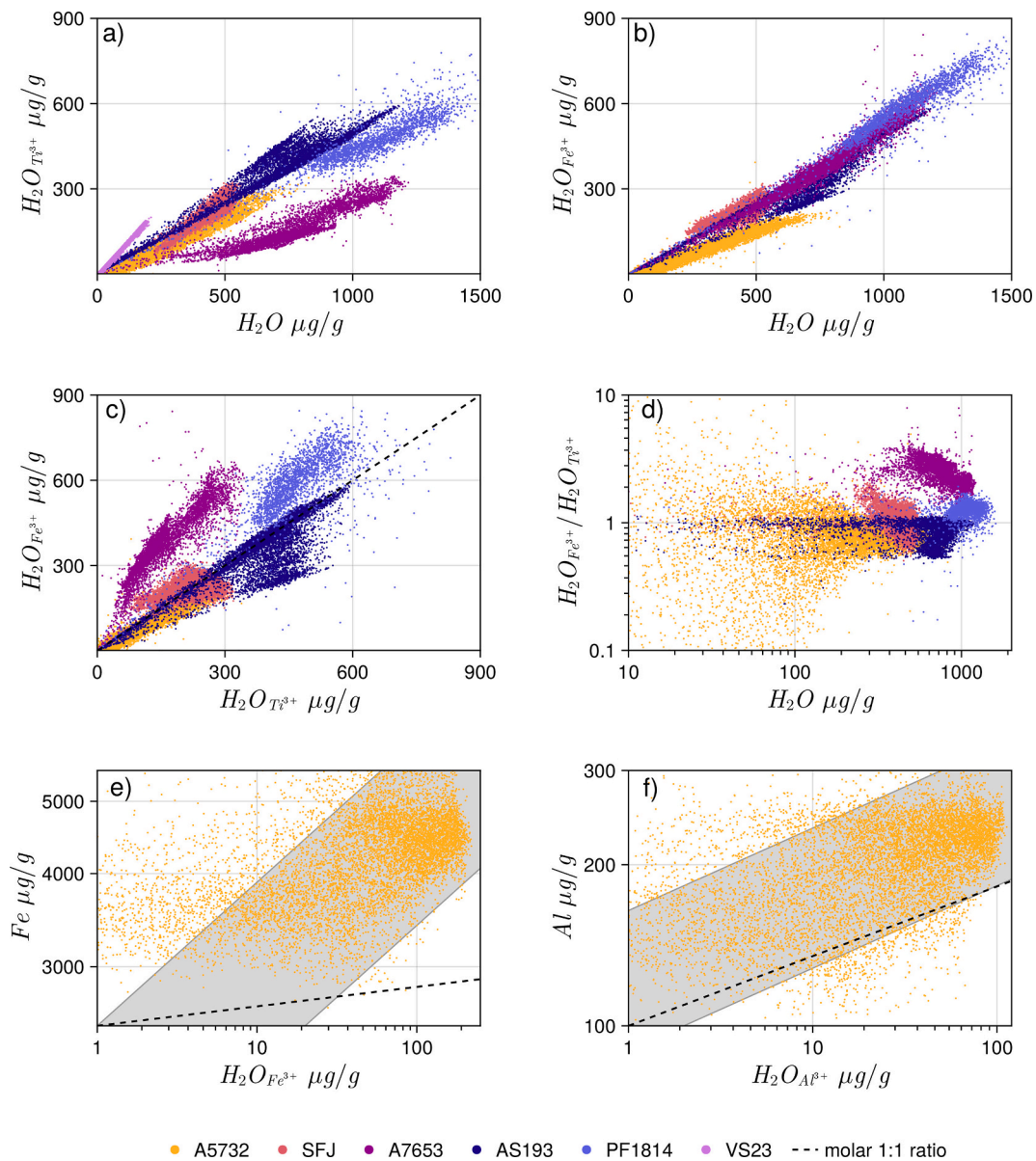


**Fig. 6.** Total- and trace element related  $H_2O$  correlation plots, for each pixel from superimposed trace element and  $H_2O$  maps. a)  $Ti^{3+}$ -related  $H_2O$  vs. total  $H_2O$  for samples A5732, SFJ, A7653, AS19-3, PF18-14, and VS23, b)  $Fe^{3+}$ -related  $H_2O$  vs. total  $H_2O$  for samples A5732, SFJ, A7653, AS19-3, PF18-14. c)  $Fe^{3+}$ - vs.  $Ti^{3+}$ -related  $H_2O$  for samples A5732, SFJ, A7653, AS19-3, and PF18-14. The black dashed line indicates a 1:1 ratio between both trace-element related  $H_2O$  contents. d)  $Fe^{3+}$ -/ $Ti^{3+}$ -related  $H_2O$  ratio vs. total  $H_2O$  for samples A5732, SFJ, A7653, AS19-3, and PF18-14. e) Fe vs  $Fe^{3+}$ -related  $H_2O$  for sample A5732. f) Al vs.  $Al^{3+}$ -related  $H_2O$  for sample A5732. The black dashed lines in e) and f) represent a molar 1:1 ratio of Fe over  $Fe^{3+}$ -related  $H_2O$  and Al over  $Al^{3+}$ -related  $H_2O$ , respectively, as can be expected for total charge balance. The intercepts are offset by 2500  $\mu g/g$  Fe ( $\sim 45$   $\mu mol/g$ ) and 100  $\mu g/g$  Al ( $\sim 4$   $\mu mol/g$ ), respectively. The grey bars show the general data trends. Each point represents one pixel in the FTIR maps (a-d), or one pixel in superimposed LA-ICP-MS and FTIR maps (e, f), respectively.

patterns in trace element-related H<sub>2</sub>O maps appearing very similar to total H<sub>2</sub>O maps (Figs. 2, 3, 4, 5). Visually, similar zoning patterns of H<sup>+</sup> and some trace elements can be recognized for each sample (Figs. 2, 3, 4, 5). To evaluate the degree of correlation between H<sup>+</sup> and trace elements and potential preferred coupling of different trace elements with H<sup>+</sup> and consequent implications for charge balance in rutile, H<sub>2</sub>O maps were superimposed on trace-element maps. The resulting transformed H<sub>2</sub>O maps allow for a pixel-by-pixel one-to-one correlation of H<sub>2</sub>O<sup>-</sup>, trace element relates H<sub>2</sub>O<sup>-</sup> and trace element contents (Fig. 6).

Total H<sub>2</sub>O contents are linearly correlated with Ti<sup>3+</sup>- and Fe<sup>3+</sup>-related H<sub>2</sub>O contents (Fig. 6a, b). Slopes of Fe<sup>3+</sup>-related H<sub>2</sub>O contents vs. total H<sub>2</sub>O contents are very similar for all analyzed samples, whereas slopes of Ti<sup>3+</sup>-related H<sub>2</sub>O contents vs. total H<sub>2</sub>O contents vary more broadly. Most samples do not have a 1:1 ratio of Ti<sup>3+</sup>-related and Fe<sup>3+</sup>-related H<sub>2</sub>O (Fig. 6c). Sample SFJ is the only rutile showing on average a molar 1:1 ratio of Ti<sup>3+</sup>-related and Fe<sup>3+</sup>-related H<sub>2</sub>O, with some areas having preferentially higher Ti<sup>3+</sup>-related H<sub>2</sub>O and other areas having slightly higher Fe<sup>3+</sup>-related H<sub>2</sub>O contents. In rutile from samples A7653 and PF18–14, H<sup>+</sup> is preferentially coupled with Fe<sup>3+</sup> over Ti<sup>3+</sup>, whereas in sample AS19–3H<sup>+</sup> is preferentially coupled with Ti<sup>3+</sup>. Sample A5732 shows a slight preference of Ti<sup>3+</sup>-related H<sup>+</sup> over Fe<sup>3+</sup>-related H<sub>2</sub>O. This relates to different ratios of Fe<sup>3+</sup>-related H<sub>2</sub>O over Ti<sup>3+</sup>-related H<sub>2</sub>O ( $H_2O_{[Fe^{3+}]}/H_2O_{[Ti^{3+}]}$ ). It has been proposed that the  $H_2O_{[Fe^{3+}]}/H_2O_{[Ti^{3+}]}$  ratio might be indicative of redox conditions under which rutile formed, as Fe<sup>3+</sup> can be expected in oxidized systems, whereas Ti<sup>3+</sup> would be expected in reduced settings (Lueder et al., 2023). Plotting the  $H_2O_{[Fe^{3+}]}/H_2O_{[Ti^{3+}]}$  ratios against total H<sub>2</sub>O contents shows the high variability of the  $H_2O_{[Fe^{3+}]}/H_2O_{[Ti^{3+}]}$  ratio (Fig. 6d). In pegmatitic sample A5732 the  $H_2O_{[Fe^{3+}]}/H_2O_{[Ti^{3+}]}$  ratio even shows preferred coupling of H<sup>+</sup> with Fe<sup>3+</sup> or Ti<sup>3+</sup> in different zones of the sample. For the  $H_2O_{[Fe^{3+}]}/H_2O_{[Ti^{3+}]}$  ratio to be dependent solely on redox conditions (i. e., oxygen fugacity), it would be expected that the  $H_2O_{[Fe^{3+}]}/H_2O_{[Ti^{3+}]}$  ratio is mostly constant throughout one sample or shows a clear zonation dependence (e.g., core-rim-zoning). If this is not the case, as can be observed in all samples, the  $H_2O_{[Fe^{3+}]}/H_2O_{[Ti^{3+}]}$  ratio must be controlled by other factors instead of, or in addition to, oxygen fugacity. Hence, the  $H_2O_{[Fe^{3+}]}/H_2O_{[Ti^{3+}]}$  ratio is not likely a viable proxy for redox conditions during rutile formation.

A complete charge balance of trace elements by related H<sup>+</sup> would lead to a molar 1:1 correlation of H<sup>+</sup> and the related trace element (e.g., Fe<sup>3+</sup>, Al<sup>3+</sup>), which is not observed for any sample (e.g., A5732 Fig. 6 e, f; Supplementary material E). Thus, Fe and Al are always coupled with H<sup>+</sup> as well as pentavalent cations and/or oxygen vacancies. For samples SFJ and A7653 multiple data clusters can be observed due to sector zoning (Supplementary material E2, E3).

For sample A5732 we observe a large spread in the data, though a general correlation of Fe and Fe<sup>3+</sup>-related H<sub>2</sub>O contents can be observed, as well as for Al and Al<sup>3+</sup>-related H<sub>2</sub>O (Fig. 6e, f). The general trends of the data clusters show a steep slope for Fe vs. Fe<sup>3+</sup>-related H<sub>2</sub>O content (Fig. 6e) and a slope that is approximately parallel to the molar 1:1 correlation for Al vs. Al<sup>3+</sup>-related H<sub>2</sub>O content (Fig. 6f). Thus, Fe in sample A5732 is preferentially coupled with pentavalent cations and/or oxygen vacancies, whereas Al has no preferred coupling. However, for both Fe and Al, the trends are shifted towards higher trace element contents than predicted by the molar 1:1. This might represent the solubility of trivalent cations into rutile at the given *P-T-X* conditions in the absence of H<sup>+</sup>. Additionally, the data clusters taper at higher Fe<sup>3+</sup>- and Al<sup>3+</sup>-related H<sub>2</sub>O contents, suggesting that the partitioning of a given trace element into rutile might have more influence on trace element coupling at low H<sub>2</sub>O contents.

Equivalently, negative correlations between pentavalent cations and H<sub>2</sub>O could be expected, as they compete for trivalent cations. Some samples show a negative correlation in Nb-H<sub>2</sub>O plots, if any correlation can be observed at all. The slope for Nb vs. H<sub>2</sub>O in sample A5732 is relatively flat, whereas in sample A7653 the slope is much steeper. The vein-related sample AS19–3 also shows a general steep, negative

correlation between Nb and H<sub>2</sub>O. Thus, it can be concluded that Nb has a significant contribution to charge balance in samples A7653 and AS19–3. Sample A5732 has a significant W content which largely contributes to charge balance. Molar charge balance calculations (Supplementary Material F) show that there is a significant charge deficit due to the presence of trivalent cations, which requires  $\sim 0.9 \times 10^{-3}$  a.p.f.u. of oxygen vacancies in sample A5732. Sample AS19–3 requires slightly more oxygen vacancies at  $\sim 1.2 \times 10^{-3}$  a.p.f.u. Oxygen vacancies are more abundant in areas of high trace-element contents and correlation plots of trivalent cations and oxygen vacancies show that Fe in samples A5732 and A7653 are preferentially coupled with oxygen vacancies over penta- and hexavalent cations or H<sup>+</sup>. However, in some areas of sample A5732, approximately 35 % of all trivalent cations are charge balanced by oxygen vacancies. Thus, understanding processes forming oxygen vacancies in rutile are vital for understanding trace-element and H<sub>2</sub>O systematics. We conclude that H<sup>+</sup> and trace element incorporation into rutile and the formation of oxygen vacancies in rutile are correlated processes.

#### 4.3. Implications for H<sup>+</sup> and trace element diffusion in rutile

Diffusive H<sup>+</sup> loss can be evaluated by plotting Fe<sup>3+</sup>-related vs. Ti<sup>3+</sup>-related H<sub>2</sub>O contents (Fig. 6c). If no H<sup>+</sup> diffusion occurs, H<sub>2</sub>O contents in the two defects are expected to show a linear correlation, as can be seen for trace element related vs. total H<sub>2</sub>O contents (Fig. 6a, b). If both Fe<sup>3+</sup>- and Ti<sup>3+</sup>-related H<sup>+</sup> diffuses, a large spread of data, away from a linear correlation would be expected. If Fe<sup>3+</sup>- related or Ti<sup>3+</sup>-related H<sup>+</sup> diffuses preferentially, a shift of the intercept away from 0 µg/g towards higher Ti<sup>3+</sup>-related or Fe<sup>3+</sup>-related H<sub>2</sub>O contents, respectively, would be observed.

All investigated samples show a linear correlation of Fe<sup>3+</sup>- related and Ti<sup>3+</sup>- related H<sub>2</sub>O contents, without large degrees of spread or shift away from the 0 intercept (Fig. 6c). Thus, the initial H<sup>+</sup> content is most likely retained in the investigated samples, without any diffusive re-equilibration after growth. All samples formed at relatively high temperatures of  $\sim 450$ – $900$  °C, significantly above the expected closure temperatures (i.e., temperatures below which trace element diffusion is no longer significant) for H<sup>+</sup> in rutile of  $< 0$  °C (e.g., Caskey, 1974; Johnson et al., 1975; Cathcart et al., 1979; Lueder et al., 2024). This H<sup>+</sup> retentivity can be explained by coupling of H<sup>+</sup> and trace elements, as has been demonstrated by Joachim-Mrosko et al. (2024). As H<sup>+</sup> is incorporated through coupled substitution with di- and trivalent cations, H<sup>+</sup> loss would create a charge deficit. To regain charge balance, coupled diffusion of H<sup>+</sup> with tri-, tetra-, or pentavalent cations (e.g.  $Fe^{3+} + H^+ \rightarrow Ti^{4+}$ ;  $2Fe^{3+} + 2H^+ \rightarrow Fe^{3+} + Nb^{5+}$ ;  $Fe^{3+} + H^+ + Ti^{4+} \rightarrow Fe^{3+} + Nb^{5+}$ ) or the formation of oxygen vacancies (e.g.  $[Fe^{3+}H^+]_2O_4 \rightarrow [Fe^{3+}]_2O_3$ ) would be required. Diffusion of tri-, tetra-, and pentavalent cations as well as oxygen in rutile is significantly slower and has higher closure temperatures (e.g., Sasaki et al., 1985; Moore et al., 1998; Cherniak et al., 2007; Marschall et al., 2013; Dohmen et al., 2019; Lueder et al., 2024). As H<sup>+</sup>-loss requires coupled diffusion for charge balance, diffusion of H<sup>+</sup> should be limited to diffusion rates of the much slower diffusing species, i.e., other cations and/or oxygen, and their expected higher closure temperatures. Based on this coupling effect, closure temperatures can be expected to be in a range of 600–750 °C for grain sizes of 50–250 µm and cooling rates of 1–100 °C/Ma (Lueder et al., 2024). For rutile of larger grain sizes, such as hydrothermal-, pegmatitic, or vein-related rutile grains, even higher closure temperatures could be expected.

A significant proportion of H<sup>+</sup> in rutile is coupled to Ti<sup>3+</sup>. The exchange  $Ti^{3+} + H^+ \rightarrow Ti^{4+}$  does not require the above discussed coupled diffusion and closure temperatures for Ti interdiffusion are in a range of  $\sim 300$ – $400$  °C (Hoshino et al., 1985). However, deconvoluted FTIR maps of Ti<sup>3+</sup>-related H<sup>+</sup> show that zoning is preserved. Thus, even this defect does not completely homogenize by diffusion, even in amphibolite-facies samples that experienced 500–600 °C. Understanding the

controlling mechanism for this observation would require further investigation through experimental studies on coupled substitution mechanisms and verification on natural rutile.

Trace-element zonation in all samples formed  $<600^\circ\text{C}$  is preserved, as closure temperatures are typically above peak metamorphic temperatures. Several experimental studies investigated trace-element diffusion in rutile, suggesting closure temperatures for Zr of  $\sim 500\text{--}700^\circ\text{C}$  (Cherniak et al., 2007; Dohmen et al., 2019), for Al of  $\sim 1000\text{--}1050^\circ\text{C}$  (Cherniak and Watson, 2019), for Fe of  $\sim 120\text{--}220^\circ\text{C}$  (Sasaki et al., 1985), and for Nb of  $\sim 550\text{--}710^\circ\text{C}$  (Marschall et al., 2013; Dohmen et al., 2019), at cooling rates of  $1\text{--}100^\circ\text{C}/\text{Ma}$  and grain sizes of  $50\text{--}250\ \mu\text{m}$ . For natural rutile, it was shown that diffusivities of Fe and Al behave similarly, with closure temperatures of Al in rutile in a range of  $675\text{--}775^\circ\text{C}$  (Joachim-Mrosko et al., 2024). As similar zoning patterns can be observed for Al, Sc, V, Cr, Fe, Zr, Nb, Sn, Ta, W, and U, it is likely that most trace-elements have closure temperatures in a range of  $\sim 500\text{--}750^\circ\text{C}$  for cooling rates of  $1\text{--}100^\circ\text{C}/\text{Ma}$  and grain sizes of  $50\text{--}250\ \mu\text{m}$ . As Fe is only zoned in fast growing pegmatitic rutile, where growth rates can be faster than diffusion rates, as well as relatively low- $T$  hydrothermal rutile, relatively lower closure temperatures as suggested by experimental data of Sasaki et al. (1985) could be feasible. Vanadium in samples AS19–3 and PF18–14 shows a less pronounced zonation compared to other trace elements. This might indicate a lower closure temperature ( $<500^\circ\text{C}$ ) resulting in (partial) diffusive equilibration of V in these samples. In the high- $T$  sample VS23, all trace elements are homogeneous, with Zr and U maps showing evidence of zircon exsolutions. This phenomenon has been described before by Meyer et al. (2011), Ewing et al. (2013) and Pape et al. (2016), who proposed that rutile formed at high temperatures of  $\sim 900\text{--}950^\circ\text{C}$  and subsequently cooled. During cooling the peak Zr contents in rutile were exsolved forming sub-micron sized zircon. This process protects the rutile grain from Zr-loss in areas with exsolutions, whereas zircon-free areas within the same grain can diffuse freely. Consequently, areas of rutile with zircon exsolutions are able to “preserve” peak Zr contents.

Generally, coupling between  $\text{H}^+$  and trace elements protects rutile from  $\text{H}^+$ -loss at temperatures below  $\sim 600\text{--}750^\circ\text{C}$ , whereas at higher temperatures,  $\text{H}^+$  and other trace elements can be diffusively lost, potentially affecting common applications of rutile trace element contents, such as Zr-in-rutile thermometry or Nb/Ta ratios.

#### 4.4. Rutile classification

Detrital rutile is commonly classified into mafic and felsic based on Cr and Nb contents (e.g., Meinhold et al., 2008). High Nb contents ( $> 800\ \mu\text{g/g}$ ) and a Cr/Nb ratios below 1 are typical for rutile from felsic/metapelitic lithologies, whereas mafic rutile has either low Nb contents ( $< 800\ \mu\text{g/g}$ ) or Cr/Nb ratios above 1. Applying this to our samples might allow to identify fluid sources for hydrothermal and vein-related rutile (Fig. 7a). The mafic eclogite PF18–14, the metapelitic granulite-facies sample VS23 and the two pegmatitic samples A5732 and SFJ plot into the expected fields. The vein-related samples M-E2, M-Q1, and PF21–02, which come from quartz-veins that are associated with mafic eclogites, have low Nb contents ( $< 800\ \mu\text{g/g}$ ), thus plotting in the mafic field. Vein-forming fluids are, therefore, likely derived or in equilibrium with the surrounding eclogite. The hydrothermal rutile A7653 has Cr/Nb ratios below 1 and very high Nb contents ( $> 5000\ \mu\text{g/g}$ ), thus plotting in the felsic field. The sample comes from an alpine cleft within a micaschist, making it likely that the hydrothermal fluid is regionally sourced or has re-equilibrated with the country rock. The vein sample AS19–1 has Cr/Nb ratios below 1 and high Nb contents ( $> 1000\ \mu\text{g/g}$ ). The host rock is a metapelite, showing that the fluid precipitating vein-rutile was in equilibrium with the country rock. Sample AS19–3 falls both into the felsic and mafic fields. The rim of the sample has high Nb contents ( $> 800\ \mu\text{g/g}$ ) and Cr/Nb ratios below 1, thus the co-existing fluid was likely mainly in equilibrium with the metapelitic host. Chromium and Nb contents of hydrothermal and vein-related rutile can

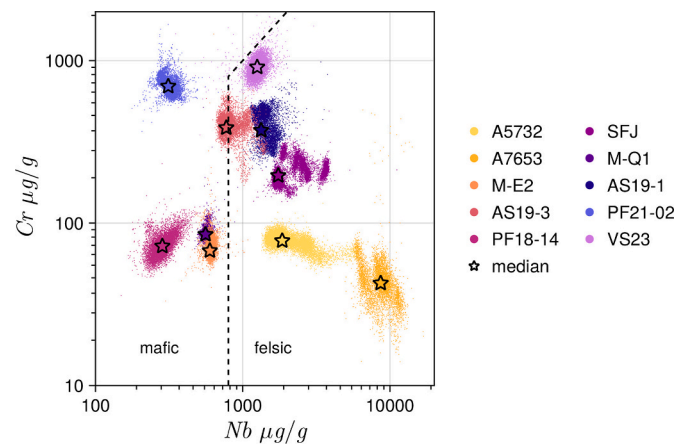


Fig. 7. Correlation plot for Cr vs. Nb of all investigated samples. Each point represents one pixel in LA-ICP-MS maps. The boundary between mafic and felsic rutile is according to Meinhold et al. (2008). The stars represent median values over the entire map.

indicate whether rutile-forming fluids are in equilibrium with the vein host rock and might track the evolution of such equilibria or non-equilibrium conditions.

#### 4.5. Zr-in-rutile thermometry

Zirconium-in-rutile thermometry uses the temperature and pressure dependent incorporation of Zr into rutile to estimate temperature conditions of rutile growth (e.g., Zack et al., 2004a; Tomkins et al., 2007; Kohn, 2020). The thermometer is widely applied and very well calibrated, allowing for precise temperature determinations in rutile-zircon-quartz-bearing metamorphic rocks. However, the thermometer has its limitations. Taylor-Jones and Powell (2015) showed that re-equilibration of Zr, Ti, and Si in the rutile-zirconium-quartz system can be limited during cooling from high temperatures, due to high closure temperatures for Si-diffusion in rutile, slow grain boundary diffusion, and restricted zircon nucleation. This would potentially lead to rutile recording temperatures above the closure temperature for Zr in rutile, but below the peak metamorphic temperature, i.e. temperature at the peak pressure, giving the impression of a too low peak metamorphic temperature. Mapping of Zr in rutile is the best way to identify zones with the highest Zr content, which would provide the best estimates for peak metamorphic temperatures. It has also been shown that Zr-in-rutile thermometry and fluid inclusion thermometry in hydrothermal rutile result in different temperature estimates (Cabral et al., 2015). The authors suggested that even though equilibrium between zircon and rutile is possible at relatively low temperature hydrothermal conditions, high fluid-rock ratios in hydrothermal systems could result in non-Zr-buffered conditions, invalidating the conditions for Zr-in-rutile thermometry (Cabral et al., 2015).

As Zr-in-rutile thermometry is only applicable to zirconium buffered systems, only samples containing zircon are considered; these are two metamorphic samples (PF18–14, VS23), the two amphibolite-facies veins (AS19–1, AS19–3), and both pegmatitic samples (A5732, SFJ). The pegmatite samples are only single rutile grains of which we do not know the rock assemblage; however, we argue that the assumption of zircon presence in a pegmatite is reasonable, as pegmatites are highly differentiated felsic melts that should contain abundant zirconium. The hydrothermal sample A7653 and the vein rutile PF21–02 are not considered, as it cannot be determined whether zircon is present, and the vein rutile M-E2 and M-Q1 do not contain zircon. Additionally, silica buffering needs to be considered. All samples containing zircon also contain quartz, thus can be used for Zr-in-rutile thermometry following the calibration of Kohn (2020). This method can yield a high precision of

$\sim \pm 5$  °C ( $2\sigma$ ) and has an accuracy of 10–15 °C. As we consider calculated temperatures and temperature variations within one grain, the accuracy can be neglected and we report errors as  $2\sigma$  standard deviations from counting statistics.

Sample A5732 has relatively homogeneous Zr contents of  $230 \pm 12$   $\mu\text{g/g}$  (Fig. 2c). Assuming pressures for melt emplacement in the crust of 0.7 GPa (Simmons and Webber, 2008), this would yield Zr-in-rutile temperatures of  $584 \pm 4$  °C. Emplacement temperatures for pegmatites are in a range of 500–600 °C, thus it is likely that Zr-in-rutile temperatures reflect magma emplacement temperatures for this pegmatitic sample.

Zirconium in the pegmatitic sample SFJ shows strong sector zoning (Fig. 2i), correlating with other trace elements. The different sectors would result in calculated temperatures of  $470 \pm 3$  °C,  $486 \pm 3$  °C, and  $492 \pm 3$  °C. The difference between lowest and highest sectors are not within the precision of  $\pm 5$  °C of the thermometer. We conclude that in this case, Zr-in-rutile thermometry is not necessarily accurate, as variations in Zr content may not reflect temperature variations but are rather a consequence of different trace element incorporation in sector zoning.

The metamorphic sample VS23 show needle-like features of high Zr and U contents that are interpreted as sub-microscopic zircon exsolutions. Apart from the exsolutions, the grain is fairly homogeneous in Zr contents ( $2390 \pm 170$   $\mu\text{g/g}$ ), equivalent to a Zr-in-rutile temperature of  $850 \pm 10$  °C (Fig. 8a). This is consistent with cooling temperatures observed for this locality (e.g., Ewing et al., 2013). If data equivalent to LA-ICP-MS spot measurements is extracted from the area with zircon exsolutions, the calculated average temperatures can yield up to  $950 \pm 80$  °C. This is similar to reported peak temperatures of the area (Ewing et al., 2013). Thus, we confirm the observation of Ewing et al. (2013) and Pape et al. (2016) that rutile grains can record both peak temperatures and cooling temperatures if the formation of zircon exsolutions is able to hinder the diffusive loss of Zr from the rutile grain to the outer matrix of the rock.

The vein rutile AS19-1 shows higher Zr contents in the core than at the rim, that relate to a temperature decreases of 20 °C from  $484 \pm 5$  °C to  $463 \pm 1$  °C (e.g., Fig. 8b). The temperatures calculated for both rutile core and rim are very close to the peak metamorphic temperature of  $475 \pm 25$  °C (Bissig and Hermann, 1999). This can be explained in three possible ways: (i) Rutile formed close to the metamorphic peak and subsequently lost Zr by diffusion, preserving peak metamorphic temperatures only in the core; (ii) Rutile-bearing veins grew retrograde

during exhumation and cooling, with Zr-in-rutile depicting the cooling path; (iii) Rutile grew at peak metamorphic temperatures, but during rutile growth, Zr was no longer buffered, resulting in Zr undersaturation and consequently lower Zr incorporation than would be expected.

In the case of sample AS19-1, Zr zoning with a relatively sharp boundary between core and rim does not resemble diffusive Zr loss or continuous retrograde rutile growth. A two-stage growth at different temperatures could explain the Zr zoning. However, Zr-contents even in the core are slightly patchy. This might indicate that variations in Zr content reflect disequilibrium growth or conditions of Zr undersaturation in the vein forming fluid. Assuming constant formation temperature and pressure it is possible to express the variations in Zr content as variations in Zr activity. The Zr activity can be expressed as ratio of actual content over expected content:

$$a_{\text{Zr}} = C_{\text{Zr}} / C_{\text{Zr}}^{T_{\text{max}}} \quad (1)$$

With  $a_{\text{Zr}}$  as Zr-activity,  $C_{\text{Zr}}$  the measured Zr content, and  $C_{\text{Zr}}^{T_{\text{max}}}$  the expected Zr content at the formation temperature and pressure. Kooijman et al. (2012) described Zr profiles in rutile from the Pikwitonei Granulite Domain, Canada, which show a decreasing Zr content within the rutile moving away from the contact of rutile towards a neighboring garnet grain. This zonation results in a large calculated temperature variability of 725–780 °C. The slow cooling rate of the granulite terrain of  $\sim 1$  °C/Ma (Kooijman et al., 2010) would result in  $\sim 40$  Ma growth duration for rutile growth during retrogression, which the authors state to be highly unlikely. Consequently, they attribute the Zr zoning to be dependent on Zr-activity, with Zr diffusion within the rock matrix being slower than rutile growth. Thus, limited Zr-availability or  $a_{\text{Zr}} < 1$  can be expressed by different zoning patterns in rutile.

Sample AS19-3 has similarly complex growth zoning as sample AS19-1, with highly variable Zr contents, with no clear core-to-rim trend. Both samples come from the same locality and show maximum Zr contents corresponding to temperatures of  $480 \pm 5$  °C, with some areas yielding Zr-activities as low as 0.7 (Fig. 8c, d). Another cause of cloudy zoning and complex zoning patterns could be inheritance from precursor phases. This is well known for e.g. Cr in garnet (e.g., Baxter et al., 2017, and references therein). In the case of rutile AS19-3, this may have been matrix rutile entrained into the quartz vein during formation.

Cloudy zoning in metamorphic sample PF18-14 also may be caused by inheritance. As rutile likely formed as pseudomorph after ilmenite, the original Zr composition of ilmenite could have been inherited by

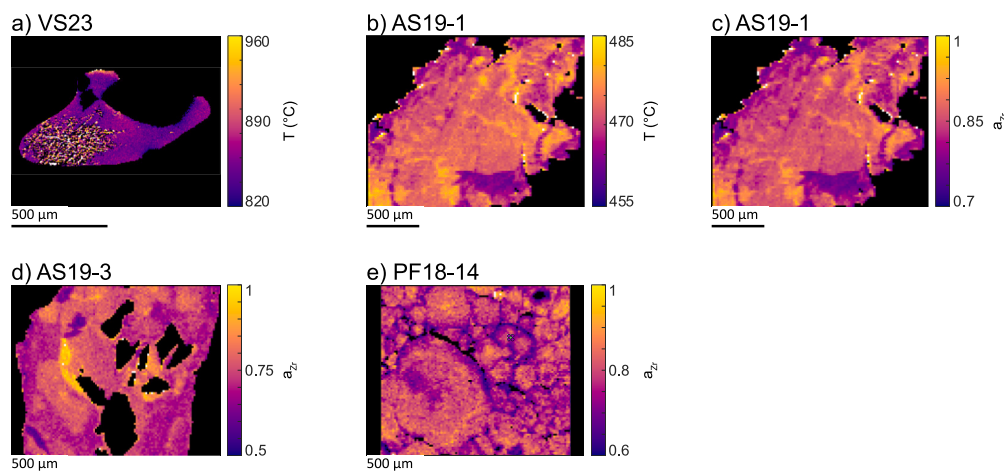


**Fig. 8.** Zr-in-rutile temperature and activity maps. Maps are calculated using the Zr-in-rutile thermometer calibrated by Kohn (2020). a) Temperature map for metamorphic sample VS23, calculated at peak-pressure of 0.8 GPa. b) Temperature map for vein-related sample AS19-1, calculated at peak-pressure of 1.0 GPa. c) Zr-activity map for sample AS19-3, calculated at peak-temperature of 485 °C. d) Zr-activity map for sample AS19-3, calculated at peak-pressure of 1.0 GPa and calculated peak-temperatures of 495 °C. e) Zr-activity map for metamorphic sample PF18-14, calculated for peak-pressure of 2.1 GPa and calculated temperatures of 500 °C. White areas in are above the maximum value of the color bar.

rutile, due to low intracrystalline diffusivity of Zr. To alter this signature, Zr would subsequently need to be diffusively re-equilibrated. However, the large volume fraction of approximately 15 vol% rutile in this rock compared to likely less than 0.1 vol% zircon, together with slow diffusion rates of Zr in rutile (Dohmen et al., 2019), makes complete re-equilibration unlikely. Therefore, Zr zoning most likely reflects inheritance with minor re-equilibration. Thus, calculated temperatures of 475–500 °C, with a median of  $485 \pm 5$  °C, are significantly below peak metamorphic temperatures of 550–600 °C and reflect significant Zr-undersaturation (Fig. 8e).

Overall, the differences in Zr content caused by potential Zr undersaturation are minor and temperatures calculated through Zr-in-rutile thermometry often overlap within the uncertainty of the method. Thus, identifying Zr zoning might have more significance for identifying other factors during rutile growth. It is evident that variations in Zr content in rutile are not necessarily related to temperature variations during rutile growth, but rather can be caused by a variety of different factors. As trace element mapping of rutile is not always feasible due to generally small grain sizes, Zr-Nb-diagrams could be a useful tool to identify factors causing variability of Zr contents in rutile. In pegmatitic and hydrothermal samples with strong oscillatory or sector zoning, we observe different clusters of Nb and Zr contents, related to different zones. This is more pronounced in samples SFJ and A7653 with sector zoning showing six and four clusters (Supplementary material C1b, c), compared to pegmatitic sample A5732 with one main cluster and only few data points forming a second group (Supplementary material C1a). For sample AS19–1, a general positive correlation between Zr and Nb can be seen, although there is significant noise in the data (Supplementary material C1f). The sample records a two-stage growth during retrogression, which is reflected in two parallel and overlapping data clusters. Metamorphic sample PF18–14 shows a data cloud, with no observable trends but rather an almost normal-distribution of Nb and Zr contents (Supplementary material C1i). This is well in line with the interpretation that Zr contents are not purely temperature dependent but also depend mainly on Zr availability. For sample AS19–3, a general dispersion of data can be observed, with a small cluster showing a correlation of Nb and Zr.

Three general types of trends in Zr–Nb diagrams can be distinguished (Fig. 9): i) Zr and Nb contents are not correlated, but rather show a general dispersion (Fig. 9b), which indicates that Zr contents are dependent on Zr availability or Zr inheritance (samples AS19–1, AS19–3, PF1814). ii) Zr and Nb show a general positive correlation (Fig. 9c) indicating diffusive alteration and thus preservation of cooling temperatures (sample VS23). iii) multiple clusters of Zr and Nb can be seen (Fig. 9d), which indicates sector- or oscillatory zoning and Zr incorporation dependent on textural controls (sample A5732). For rutile grains recording peak temperatures, it would be expected that Zr contents are nearly invariant, whereas Nb contents can be variable, resulting in near-horizontal lines, with only minor scatter in Zr vs Nb plots. As oscillatory zoning, sector zoning and Zr-undersaturation can be readily identified, this classification might function as a first order approximation in cases where trace element mapping is not feasible to evaluate whether Zr-in-rutile thermometry can be reliably applied.

#### 4.6. Nb–Ta contents and Nb/Ta ratio

Rutile is a main host of HFSE, and rutile Nb/Ta ratios are expected to represent bulk rock Nb/Ta ratios. As Nb/Ta ratios can be used to infer geochemical reservoirs (e.g., Foley et al., 2000; Rudnick et al., 2000; Stepanov and Hermann, 2013), rutile Nb/Ta ratios potentially can provide the same information.

The investigated samples show zonation of Nb and/or Ta, resulting in highly variable Nb/Ta ratios within each sample (Fig. 10). The vein samples M-E2, M-Q1, and PF21–02 show sector-like- or oscillatory zoning in Nb and/or Ta, resulting in the same zoning patterns in Nb/Ta ratios, with a spread of Nb/Ta ratios between 11 and 19, ranging from

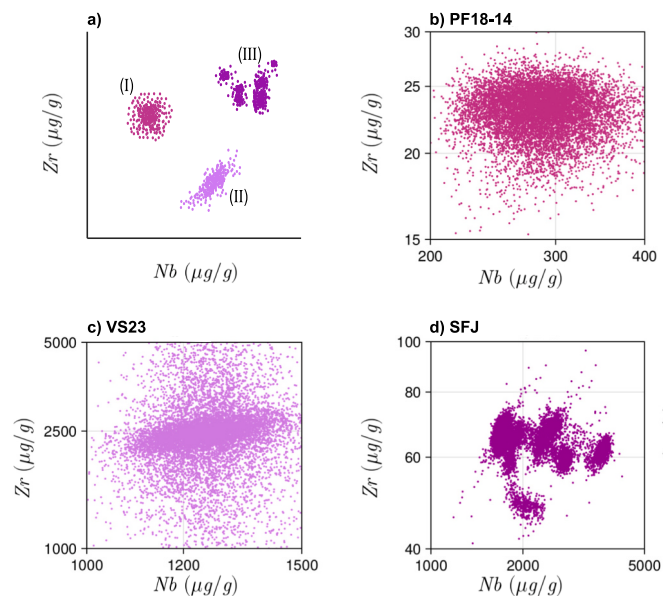


**Fig. 9.** Zr–Nb diagrams. a) Schematic sketch of data clusters in Zr–Nb diagrams. The three clusters represent: (I) dispersed data (magenta) due to a dependence on Zr availability or Zr inheritance. (II) positive correlation (pink) indicating preservation of cooling temperatures. (III) multiple clusters (purple) indicating sector- or oscillatory zoning. b-d) Examples for each group from measured rutile samples. b) Metamorphic sample PF18–14 showing a pattern representative for group (I). c) Vein-related sample VS23 showing a pattern representative for group (II). d) Pegmatitic sample showing a general pattern representative for group (III). (For interpretation of the references to color in this figure legend, the reader is referred to the web version of this article.)

values typical for continental crust, over DM or MORB, up to chondritic values. Zoning in samples AS19–1 and AS19–3 also follows Nb and Ta zoning with Nb/Ta ratios from 10 to 23 and 27, respectively. These values are equivalent to values for continental crust (8–14; Rudnick and Fountain, 1995) and extend to superchondritic values known for the upper lithospheric mantle or refractory eclogite (19–37; Rudnick et al., 2000; Kalfoun et al., 2002). Metamorphic sample PF18–14 has highly patchy Nb and Ta zoning, resulting in Nb/Ta ratios between 7 and 35, spanning almost the entire range of known Nb/Ta ratios.

The pegmatitic sample SFJ shows sector zoning of Nb/Ta-ratios, with values of 8–14, typical for continental crust. However, the pegmatitic sample A5732 has extremely variable Nb/Ta ratios of 15–52, which is significantly higher than reported suprachondritic values. Hydrothermal sample A7653 has Nb/Ta ratios of 4–15. Fluids typically have low Nb/Ta ratios, which increase with increasing temperature (Schmidt et al., 2004). However, a variability of Nb/Ta ratios in this range would suggest a temperature variation of ~500–1000 °C, which is not realistic for a hydrothermal system, suggesting sector- and oscillatory zoning as the main cause for variable Nb/Ta ratios.

The spread of Nb/Ta ratios across and within samples can be best seen in Nb-Ta-diagrams (Fig. 11a, c). All mafic samples show linear correlations between Nb and Ta. However, the trends are not parallel to Nb/Ta-ratio isopleths, but Ta contents are more variable, indicating that variability of Nb/Ta-ratios depends mainly on variability of Ta, likely due to stronger fractionation of Ta in the fluid mitigated systems that have dominantly been investigated. As rutile contains >95 % of the bulk Nb and Ta, median Nb/Ta ratios of rutile should reflect the bulk rock Nb/Ta ratio. The observed zoning of Nb, Ta, and Nb/Ta ratios indicates thus that Nb and Ta do not behave fully as geochemical twins but can fractionate during rutile growth. One possible explanation for this fractionation might be different transport mechanisms of Nb and Ta in the intermedium due to their mass difference. The differences in Nb and Ta diffusion in rutile itself (Dohmen et al., 2019) are not a reasonable

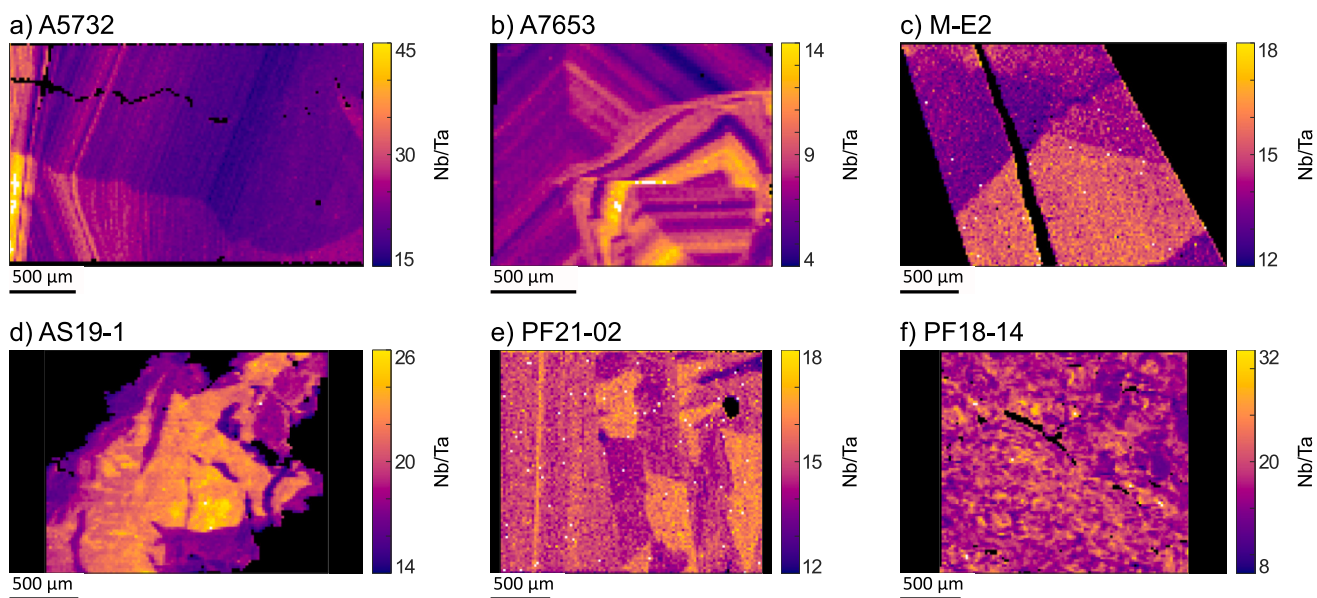


Fig. 10. Nb/Ta-ratio maps for selected samples. Calculated from Nb and Ta maps. White areas are above the maximum value of the color bar.

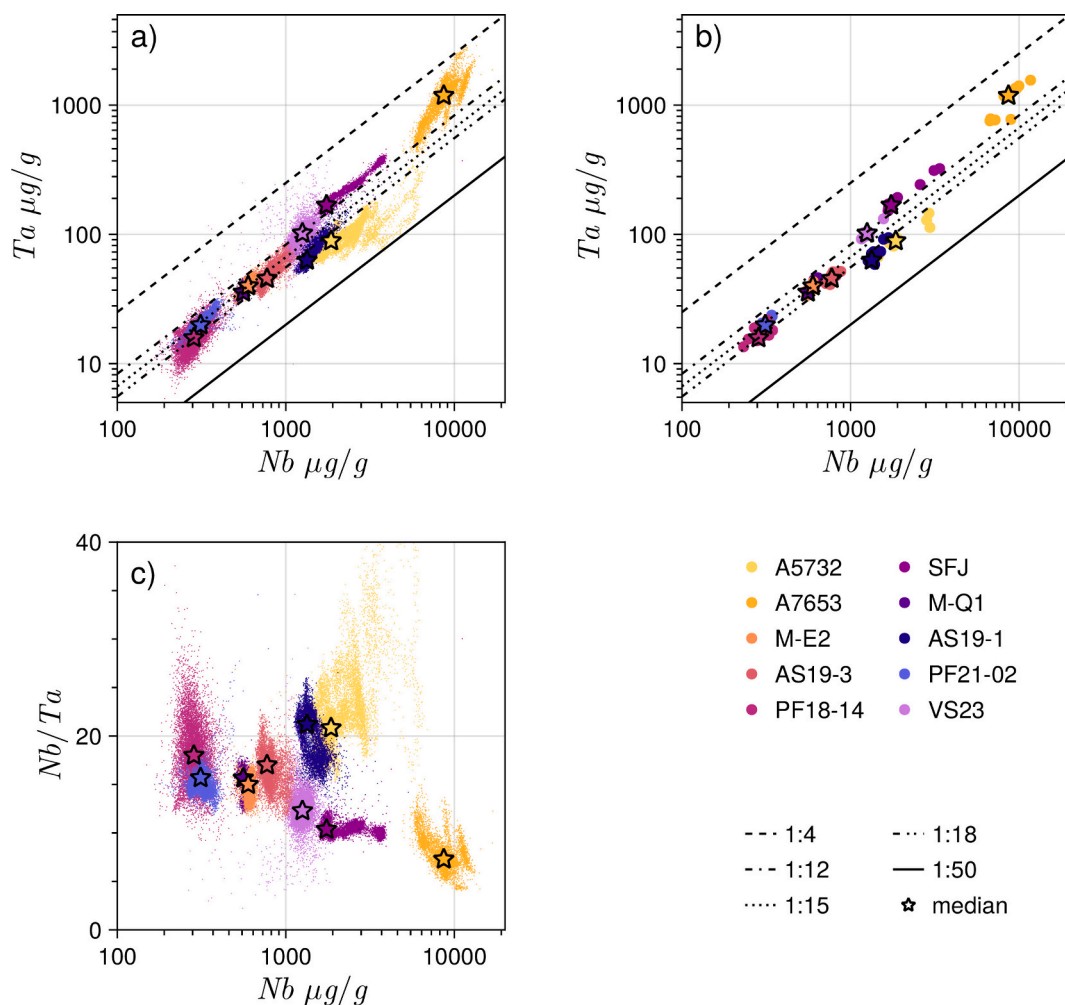


Fig. 11. Correlation plots for Ta vs. Nb of all investigated samples. a) Each point represents one pixel in LA-ICP-MS maps. b) Ta vs. Nb plot of ten randomly sampled spots for each sample. Spot positions are shown in Fig. 1 and spot data was extracted from maps in XMapTools. The boundary between mafic and felsic rutile in a) according to Meinhold et al. (2008). The black lines represent Nb/Ta-ratios of 4, 12, 15, 18, and 50, the stars represent median values over the entire maps. c) Nb/Ta ratios vs. Nb contents with each point representing one pixel in LA-ICP-MS maps.

explanation, as the investigated rutile grains formed below the closure temperatures of Nb and Ta diffusion in rutile.

To test the intra-grain variability of Nb/Ta ratios, Nb- and Ta contents of ten randomly sampled, ~70  $\mu\text{m}$ -sized spots for each sample, representing typical LA-ICP-MS spot measurements (Fig. 1, 10b; Supplementary material D) were extracted using XMapTools (Lanari and Piccoli, 2020). Generally, median Nb/Ta ratios from the entire map data are represented relatively well by extracted spots. However, extracted spots do not represent the range of Nb and Ta contents or Nb/Ta ratios that can be observed in the maps (Fig. 11), and in most samples show a significantly narrower range of Nb/Ta ratios, as can be expected from comparing a “micro-bulk” (i.e., spots) to higher resolution data (i.e., maps). The range between Nb/Ta ratios of values typical for continental crust up to supra-chondritic values seen in the maps are not reflected by the spots. Similarly, sector zoning in Nb and/or Ta cannot be identified from extracted spots, as the data commonly appears scattered. Even if distinct groups of Nb and Ta contents might be recognizable, as for sample PF21-02, the small number of spots makes it much more difficult to interpret, and sector zoning might be miss-interpreted as normal metamorphic, core-rim type, linear growth zoning, as can be observed in e.g., samples AS19-1, AS19-3 and M-Q1. In the comparison of Fig. 11, significant differences of Nb/Ta ratios between the microscale (trace element maps, Fig. 11a, c) and mesoscale (spot analyses, Fig. 11b) can be seen. Spots represent the median values but do not necessarily depict the large spread observed in maps. Mapping approaches allow for a more detailed understanding of Nb and Ta incorporation into rutile and might show fractionation processes of Nb and Ta at the microscale. Therefore, mapping approaches might be useful in investigating the “missing Nb-paradox” and Nb-Ta-fractionation processes (e.g., Rudnick et al., 2000; Foley et al., 2000; Stepanov and Hermann, 2013), leading to sub-chondritic Nb/Ta ratios in most geochemical reservoirs. Additionally, if zoning patterns have similar characteristics on smaller grain scales, mapping might be a useful tool to identify source lithologies of detrital rutile, which is vital for provenance studies.

## 5. Conclusions

We investigated intra-grain variabilities of trace elements and  $\text{H}_2\text{O}$  contents in rutile for pegmatites, hydrothermal- and vein-related samples, amphibolite-facies quartz lenses, a mafic low- $T$  eclogite, and a metapelitic granulite. All samples show different, partially complex trace element and OH zoning, that seems to be largely controlled by external factors, such as availability and diffusivity within the rock matrix. The complexity of rutile trace element geochemistry that may be observed through mapping approaches offers multiple directions for future research:

- i) Trace element zoning varies between regular patterns more commonly observed in rutile from hydrothermal clefts and pegmatites and irregular zoning in rutile from high- $P$  veins and metamorphic rocks.
- ii) Zirconium contents in rutile can be highly variable and, besides the well-established temperature dependence, it can also be dependent on Zr availability (e.g., Zr activity, disequilibrium, kinetics). Mapping of Zr contents can help identify areas with the highest Zr contents, that are most likely to reflect peak metamorphic temperatures.
- iii) Nb/Ta ratios are more variable than can be seen from LA-ICP-MS single spot measurements, suggesting that mapping approaches might be a useful tool to investigate Nb-Ta fractionation processes during rutile growth.
- iv) Hydrogen is retained in low- $T$  rutile (below ~650  $^\circ\text{C}$ ), likely due to coupling of  $\text{H}^+$  with trivalent cations, which limits diffusion rates and increases closure temperatures. The  $\text{H}^+$  retentivity has implications for trace-element incorporation (e.g., preferred trace element coupling) and charge balance in rutile.

## CRediT authorship contribution statement

**Mona Lueder:** Writing – original draft, Visualization, Methodology, Investigation, Formal analysis, Data curation, Conceptualization. **Jörg Hermann:** Writing – review & editing, Supervision, Resources, Funding acquisition, Conceptualization. **Renée Tamblin:** Writing – review & editing, Investigation, Formal analysis. **Daniela Rubatto:** Writing – review & editing, Supervision, Resources. **Pierre Lanari:** Writing – review & editing, Software, Methodology. **Thorsten Andreas Markmann:** Software, Methodology, Formal analysis.

## Declaration of competing interest

The authors declare that they have no known competing financial interests or personal relationships that could have appeared to influence the work reported in this paper.

## Data availability

Data will be made available on request.

## Acknowledgements

We thank Beda Hofmann and the Natural History Museum Bern for providing samples A5732 and A7653. This work was financially supported by the Swiss Science Foundation (grant no. 200020\_196927). We thank Sonja Aulbach for her editorial work and two anonymous reviewers for their comments which helped improve this work.

## Appendix A. Supplementary data

Supplementary data to this article can be found online at <https://doi.org/10.1016/j.chemgeo.2024.122480>.

## References

- Ague, J.J., Axler, J.A., 2016. Interface coupled dissolution-precipitation in garnet from subducted granulites and ultrahigh-pressure rocks revealed by phosphorous, sodium, and titanium zonation. *Am. Mineral.* 101, 1696–1699. <https://doi.org/10.2138/am-2016-5707>.
- Barth, M.G., McDonough, W.F., Rudnick, R.L., 2000. Tracking the budget of Nb and Ta in the continental crust. *Chem. Geol.* 165, 197–213. [https://doi.org/10.1016/S0009-2541\(99\)00173-4](https://doi.org/10.1016/S0009-2541(99)00173-4).
- Baxter, E.F., Caddick, M.J., Dragovic, B., 2017. Garnet: a rock-forming mineral petrochronometer. *Rev. Mineral. Geochem.* 83, 469–533. <https://doi.org/10.2138/rmg.2017.83.15>.
- Bissig, T., Hermann, J., 1999. From pre-Alpine extension to Alpine convergence: the example of the southwestern margin of the Margna nappe (Val Malenco, N-Italy). *Schweizerische Mineral. und Petrogr. Mitteilungen* 3, 363–380.
- Bracciali, L., Parrish, R.R., Horstwood, M.S.A., Condon, D.J., Najman, Y., 2013. UPb-LA-(MC)-ICP-MS dating of rutile: New reference materials and applications to sedimentary provenance. *Chem. Geol.* 347, 82–101. <https://doi.org/10.1016/j.chemgeo.2013.03.013>.
- Bromiley, G.D., Hilaret, N., 2005. Hydrogen and minor element incorporation in synthetic rutile. *Mineral. Mag.* 69, 345–358. <https://doi.org/10.1180/0026461056930256>.
- Bromiley, G., Hilaret, N., McCammon, C., 2004. Solubility of hydrogen and ferric iron in rutile and TiO<sub>2</sub> (II): Implications for phase assemblages during ultrahigh-pressure metamorphism and for the stability of silica polymorphs in the lower mantle. *Geophys. Res. Lett.* 31 (4), 2–6. <https://doi.org/10.1029/2004GL019430>.
- Bucher, K., Fazis, Y., de Capitani, C., Grapes, R., 2005. Blueschists, eclogites, and decompression assemblages of the Zermatt-Saas ophiolite: High-pressure metamorphism of subducted Tethys lithosphere. *Am. Mineral.* 90, 821–835. <https://doi.org/10.2138/am.2005.1718>.
- Cabral, A.R., Rios, F.J., Ramos, Aparecida, de Oliveira, L., Robério de Abreu, F., Lehmann, B., Zack, T., Laufek, F., 2015. Fluid - inclusion microthermometry and the Zr - in - rutile thermometer for hydrothermal rutile. *Int. J. Earth Sci.* 104, 513–519. <https://doi.org/10.1007/s00531-014-1120-8>.
- Carocci, E., Marignac, C., Cathelineau, M., Truche, L., Lecomte, A., Pinto, F., 2019. Rutile from panasqueira (Central Portugal): an excellent pathfinder for wolframite deposition. *Minerals* 9, 13–15. <https://doi.org/10.3390/min9010009>.
- Carruzzo, S., Clarke, D.B., Pelrine, K.M., MacDonald, M.A., 2006. Texture, composition, and origin of rutile in the South Mountain Batholith, Nova Scotia. *Can. Mineral.* 44 (3), 715–729. <https://doi.org/10.2113/gscanmin.44.3.715>.

- Caskey, G.R., 1974. Diffusion of tritium in rutile (TiO<sub>2</sub>). *Mater. Sci. Eng.* 14, 109–114. [https://doi.org/10.1016/0025-5416\(74\)90003-2](https://doi.org/10.1016/0025-5416(74)90003-2).
- Cathcart, J.V., Perkins, R.A., Bates, J.B., Manley, L.C., 1979. Tritium diffusion in rutile (TiO<sub>2</sub>). *J. Appl. Phys.* 50, 4110–4119. <https://doi.org/10.1063/1.326490>.
- Cherniak, D.J., Watson, E.B., 2019. Al and Si diffusion in rutile. *Am. Mineral.* 104, 1638–1649. <https://doi.org/10.2138/am-2019-7030>.
- Cherniak, D.J., Manchester, J., Watson, E.B., 2007. Zr and Hf diffusion in rutile. *Earth Planet. Sci. Lett.* 261, 267–279. <https://doi.org/10.1016/j.epsl.2007.06.027>.
- Corfu, F., Hanchar, J.M., Hoskin, P.W.O., Kinny, P., 2003. Atlas of zircon textures. *Rev. Mineral. Geochem.* 53, 469–500. <https://doi.org/10.2113/0530469>.
- Dohmen, R., Marschall, H.R., Ludwig, T., Polednia, J., 2019. Diffusion of Zr, Hf, Nb and Ta in rutile: effects of temperature, oxygen fugacity, and doping level, and relation to rutile point defect chemistry. *Phys. Chem. Miner.* 46, 311–332. <https://doi.org/10.1007/s00269-018-1005-7>.
- Ewing, T.A., Hermann, J., Rubatto, D., 2013. The robustness of the Zr-in-rutile and Ti-in-zircon thermometers during high-temperature metamorphism (Ivrea-Verbano Zone, northern Italy). *Contrib. Mineral. Petrol.* 165, 757–779. <https://doi.org/10.1007/s00410-012-0834-5>.
- Foley, S.F., Barth, M.G., Jenner, G.A., 2000. Rutile/melt partition coefficients for trace elements and an assessment of the influence of rutile on the trace element characteristics of subduction zone magmas. *Geochim. Cosmochim. Acta* 64, 933–938. [https://doi.org/10.1016/S0016-7037\(99\)00355-5](https://doi.org/10.1016/S0016-7037(99)00355-5).
- Gies, N.B., Lanari, P., Hermann, J., 2024. A workflow and software solution for spatially resolved spectroscopic and numerical data (SpecXY). *Comput. Geosci.* 189, 105626. <https://doi.org/10.1016/j.cageo.2024.105626>.
- Giuntoli, F., Lanari, P., Engi, M., 2017. Deeply subducted continental fragments: I. Fracturing, dissolution-precipitation and diffusion processes recorded by garnet textures of the central Sesia Zone (Western Italian Alps). *Solid Earth Discuss.* 9, 167–189. <https://doi.org/10.5194/se-2017-87>.
- Graham, J., Morris, R.C., Bag, P., Laboratories, G.C., Street, P., 1973. Tungsten- and antimony-substituted rutile. *Mineral. Mag.* 39, 470–473. <https://doi.org/10.1180/minmag.1973.039.304.11>.
- Hammer, V.M.F., Beran, A., 1991. Variations in the OH concentration of rutiles from different geological environments. *Mineral. Petrol.* 45, 1–9. <https://doi.org/10.1007/BF01164498>.
- Hoshino, K., Peterson, N.L., Wiley, C.L., 1985. Diffusion and point defects in TiO<sub>2</sub>-x. *J. Phys. Chem. Solid* 46, 1397–1411. [https://doi.org/10.1016/0022-3697\(85\)90079-4](https://doi.org/10.1016/0022-3697(85)90079-4).
- Hou, Z., Xiao, Y., Shen, J., Yu, C., 2020. In situ rutile U–Pb dating based on zircon calibration using LA–ICP–MS, geological applications in the Dabie orogen, China. *J. Asian Earth Sci.* 192, 104261. <https://doi.org/10.1016/j.jseas.2020.104261>.
- Huang, J., Xiao, Y., Gao, Y., Hou, Z., Wu, W., 2012. Nb-Ta fractionation induced by fluid-rock interaction in subduction-zones: Constraints from UHP eclogite- and vein-hosted rutile from the Dabie orogen, Central-Eastern China. *J. Metam. Geol.* 30, 821–842. <https://doi.org/10.1111/j.1525-1314.2012.01000.x>.
- Jenkins, K., Goemann, K., Belousov, I., Morrissette, M., Danyushevsky, L., 2023. Investigation of the ablation behaviour of andradite-grossular garnets and rutile with implications for U–Pb geochronology. *Geostand. Geoanalytical Res.* 47, 267–295. <https://doi.org/10.1111/ggr.12478>.
- Joachim-Mrosko, B., Konzett, J., Ludwig, T., Griffiths, T., Habler, G., Libowitzky, E., Stalder, R., 2024. Al and H incorporation and Al-diffusion in natural rutile and its high-pressure polymorph TiO<sub>2</sub> (II). *Geol. Soc. London. Spec. Publ.* 537, 123–147. <https://doi.org/10.1144/sp537-2022-187>.
- Jochum, K.P., Stolz, A.J., McOrist, G., 2000. Niobium and tantalum in carbonaceous chondrites: Constraints on the solar system and primitive mantle niobium/tantalum, zirconium/niobium, and niobium/uranium ratios. *Meteorit. Planet. Sci.* 35, 229–235. <https://doi.org/10.1111/j.1945-5100.2000.tb01771.x>.
- Jochum, K.P., Weis, U., Stoll, B., Kuzmin, D., Yang, Q., Raczek, I., Jacob, D.E., Stracke, A., Birbaum, K., Frick, D.A., Günther, D., Enzweiler, J., 2011. Determination of reference values for NIST SRM 610-617 glasses following ISO guidelines. *Geostand. Geoanalytical Res.* 35, 397–429. <https://doi.org/10.1111/j.1751-908X.2011.00120.x>.
- Johnson, O.W., Ohlsen, W.D., Kingsbury, P.L., 1968. Defects in rutile. III. Optical and electrical properties of impurities and charge carriers. *Phys. Rev.* 175, 1102–1109. <https://doi.org/10.1103/PhysRev.175.1102>.
- Johnson, O.W., Paek, S.H., Deford, J.W., 1975. Diffusion of H and D in TiO<sub>2</sub>: suppression of internal fields by isotope exchange. *J. Appl. Phys.* 46, 1026–1033. <https://doi.org/10.1063/1.322206>.
- Kalfoun, F., Ionov, D., Merlet, C., 2002. HFSE residence and Nb/Ta ratios in metasomatised, rutile-bearing mantle peridotites. *Earth Planet. Sci. Lett.* 199, 49–65. [https://doi.org/10.1016/S0012-821X\(02\)00555-1](https://doi.org/10.1016/S0012-821X(02)00555-1).
- Kohn, M.J., 2020. A refined zirconium-in-rutile thermometer. *Am. Mineral.* 105, 963–971. <https://doi.org/10.2138/am-2020-7091>.
- Kohn, M.J., Penniston-Dorland, S.C., Ferreira, J.C.S., 2016. Implications of near-rim compositional zoning in rutile for geothermometry, geospeedometry, and trace element equilibration. *Contrib. Mineral. Petrol.* 171, 1–15. <https://doi.org/10.1007/s00410-016-1285-1>.
- Kooijman, E., Mezger, K., Berndt, J., 2010. Constraints on the U–Pb systematics of metamorphic rutile from in situ LA–ICP–MS analysis. *Earth Planet. Sci. Lett.* 293, 321–330. <https://doi.org/10.1016/j.epsl.2010.02.047>.
- Kooijman, E., Smit, M.A., Mezger, K., Berndt, J., 2012. Trace element systematics in granulite facies rutile: Implications for Zr geothermometry and provenance studies. *J. Metam. Geol.* 30 (4), 397–412. <https://doi.org/10.1111/j.1525-1314.2012.00972.x>.
- Lanari, P., Piccoli, F., 2020. New horizons in quantitative compositional mapping - Analytical conditions and data reduction using XMapTools. *IOP Conf. Ser. Mater. Sci. Eng.* 891, 012016. <https://doi.org/10.1088/1757-899X/891/1/012016>.
- Lueder, M., Tamblyn, R., Hermann, J., 2023. A framework for quantitative in situ evaluation of coupled substitutions between H<sup>+</sup> and trace elements in natural rutile. *Eur. J. Mineral.* 35, 243–265. <https://doi.org/10.5194/ejm-35-243-2023>.
- Lueder, M., Tamblyn, R., Rubatto, D., Hermann, J., 2024. H<sub>2</sub>O-rich rutile as an indicator for modern-style cold subduction. *Contrib. Mineral. Petrol.* 179, 26. <https://doi.org/10.1007/s00410-024-02107-2>.
- Markmann, T.A., Lanari, P., Piccoli, F., Pettke, T., Tamblyn, R., Tedeschi, M., Lueder, M., Kunz, B.E., Riel, N., Laughton, J., 2024. Multi-phase quantitative compositional mapping by LA–ICP–MS: Analytical approach and data reduction protocol implemented in XMapTools. *Chem. Geol.* 646, 121895. <https://doi.org/10.1016/j.chemgeo.2023.121895>.
- Marschall, H.R., Dohmen, R., Ludwig, T., 2013. Diffusion-induced fractionation of niobium and tantalum during continental crust formation. *Earth Planet. Sci. Lett.* 375, 361–371. <https://doi.org/10.1016/j.epsl.2013.05.055>.
- McDonough, W.F., Sun, S.-S., 1995. The composition of the Earth. *Chem. Geol.* 120, 223–253. [https://doi.org/10.1016/0009-2541\(94\)00140-4](https://doi.org/10.1016/0009-2541(94)00140-4).
- Meinhold, G., 2010. Rutile and its applications in earth sciences. *Earth-Sci. Rev.* 102, 1–28. <https://doi.org/10.1016/j.earscirev.2010.06.001>.
- Meinhold, G., Anders, B., Kostopoulos, D., Reischmann, T., 2008. Rutile chemistry and thermometry as provenance indicator: an example from Chios Island, Greece. *Sediment. Geol.* 203, 98–111. <https://doi.org/10.1016/j.sedgeo.2007.11.004>.
- Meyer, M., John, T., Brandt, S., Klemm, R., 2011. Trace element composition of rutile and the application of Zr-in-rutile thermometry to UHT metamorphism (Epupa complex, NW Namibia). *Lithos* 126 (3–4), 388–401. <https://doi.org/10.1016/j.lithos.2011.07.013>.
- Mezger, K., Hannon, G.N., Bohlen, S.R., 1989. High-precision U–Pb ages of metamorphic rutile: application to the cooling history of high-grade terranes. *Earth Planet. Sci. Lett.* 96, 106–118. [https://doi.org/10.1016/0012-821X\(89\)90126-X](https://doi.org/10.1016/0012-821X(89)90126-X).
- Moore, D.K., Cherniak, D.J., Watson, E.B., 1998. Oxygen diffusion in rutile from 750 to 1000 °C and 0.1 to 1000. *Am. Mineral.* 83, 700–711. <https://doi.org/10.2138/am-1998-7-803>.
- Münker, C., Pfänder, J.A., Weyer, S., Büchl, A., Kleine, T., Mezger, K., 2003. Evolution of planetary cores and the Earth-Moon system from Nb/Ta systematics. *Science* 301, 84–87. <https://doi.org/10.1126/science.1084662>.
- Nakamura, Y., 1973. Origin of sector-zoning of igneous clinopyroxenes. *Am. Mineral.* 58, 986–990.
- Pape, J., Mezger, K., Robyr, M., 2016. A systematic evaluation of the Zr-in-rutile thermometer in ultra-high temperature (UHT) rocks. *Contrib. Mineral. Petrol.* 171. <https://doi.org/10.1007/s00410-016-1254-8>.
- Pfänder, J.A., Münker, C., Stracke, A., Mezger, K., 2007. Nb/Ta and Zr/Hf in ocean island basalts - Implications for crust-mantle differentiation and the fate of Niobium. *Earth Planet. Sci. Lett.* 254, 158–172. <https://doi.org/10.1016/j.epsl.2006.11.027>.
- Pollok, K., Lloyd, G.E., Austrheim, H., Putnis, A., 2008. Complex replacement patterns in garnets from Bergen Arcs eclogites: a combined EBSD and analytical TEM study. *Chem. Erde* 68, 177–191. <https://doi.org/10.1016/j.chemer.2007.12.002>.
- Regis, D., Rubatto, D., Darling, J., Cenki-Tok, B., Zucali, M., Engi, M., 2014. Multiple metamorphic stages within an eclogite-facies terrane (Sesia Zone, Western Alps) revealed by Th–U–Pb petrochronology. *J. Petrol.* 55, 1429–1456. <https://doi.org/10.1093/ptrology/egu029>.
- Reynes, J., Lanari, P., Hermann, J., 2020. A mapping approach for the investigation of Ti–OH relationships in metamorphic garnet. *Contrib. Mineral. Petrol.* 175, 1–17. <https://doi.org/10.1007/s00410-020-01681-5>.
- Rice, C.M., Darke, K.E., Still, J.W., Lachowski, E.E., 1998. Tungsten-bearing rutile from the Kori Kollo gold mine, Bolivia. *Mineral. Mag.* 62, 421–429. <https://doi.org/10.1180/002646198547684>.
- Rubatto, D., Burger, M., Lanari, P., Hattendorf, B., Schwarz, G., Neff, C., Keresztes Schmidt, P., Hermann, J., Vho, A., Günther, D., 2020. Identification of growth mechanisms in metamorphic garnet by high-resolution trace element mapping with LA–ICP–TOFMS. *Contrib. Mineral. Petrol.* 175, 1–19. <https://doi.org/10.1007/s00410-020-01700-5>.
- Rudnick, R.L., Fountain, D.M., 1995. Nature and composition of the continental crust: a lower crustal perspective. *Rev. Geophys.* 33, 267–309. <https://doi.org/10.1029/95RG01302>.
- Rudnick, R.L., Barth, M., Horn, I., McDonough, W.F., 2000. Rutile-bearing refractory eclogites: Missing link between continents and depleted mantle. *Science* 287, 278–281. <https://doi.org/10.1126/science.287.5451.278>.
- Sasaki, J., Peterson, N.L., Hoshino, K., 1985. Tracer impurity diffusion in single-crystal rutile (TiO<sub>2</sub>-x). *J. Phys. Chem. Solid* 46, 1267–1283. [https://doi.org/10.1016/0022-3697\(85\)90129-5](https://doi.org/10.1016/0022-3697(85)90129-5).
- Schmidt, M.W., Dardon, A., Chazot, G., Vannucci, R., 2004. The dependence of Nb and Ta rutile-melt partitioning on melt composition and Nb/Ta fractionation during subduction processes. *Earth Planet. Sci. Lett.* 226, 415–432. <https://doi.org/10.1016/j.epsl.2004.08.010>.
- Schmitt, A.K., Zack, T., 2012. High-sensitivity U–Pb rutile dating by secondary ion mass spectrometry (SIMS) with an O<sup>2+</sup> primary beam. *Chem. Geol.* 332–333, 65–73. <https://doi.org/10.1016/j.chemgeo.2012.09.023>.
- Sciuba, M., Beaudoin, G., 2021. Texture and trace element composition of rutile in orogenic gold deposits. *Econ. Geol.* 116 (8), 1865–1892. <https://doi.org/10.5382/ECONGEO.4857>.
- Scott, K.M., 2005. Rutile geochemistry as a guide to porphyry Cu–Au mineralization, Northparkes, New South Wales, Australia. *Geochem.: Explor. Environ. Anal.* 5 (3), 247–253. <https://doi.org/10.1144/1467-7873/03-055>.

- Simmons, W.B., Webber, K.L., 2008. Pegmatite genesis: state of the art. *Eur. J. Mineral.* 421–438. <https://doi.org/10.1127/0935-1221/2008/0020-1833>.
- Skora, S., Mahlen, N.J., Johnson, C.M., Baumgartner, L.P., Lapen, T.J., Beard, B.L., Szilvagy, E.T., 2015. Evidence for protracted prograde metamorphism followed by rapid exhumation of the Zermatt-Saas fee ophiolite. *J. Metam. Geol.* 33, 711–734. <https://doi.org/10.1111/jmg.12148>.
- Stepanov, A.S., Hermann, J., 2013. Fractionation of Nb and Ta by biotite and phengite: Implications for the “missing Nb paradox.” *Geology* 41, 303–306. <https://doi.org/10.1130/G33781.1>.
- Taylor-Jones, K., Powell, R., 2015. Interpreting zirconium-in-rutile thermometric results. *J. Metam. Geol.* 33, 115–122. <https://doi.org/10.1111/jmg.12109>.
- Tollo, R.P., Haggerty, S.E., 1987. Nb-Cr-rutile in the orapa kimberlite, Botswana. *Can. Mineral.* 25, 251–264.
- Tomkins, H.S., Powell, R., Ellis, D.J., 2007. The pressure dependence of the zirconium-in-rutile thermometer. *J. Metam. Geol.* 25, 703–713. <https://doi.org/10.1111/j.1525-1314.2007.00724.x>.
- Urban, A.J., Hoskins, B.F., Grey, I.E., 1992. Characterization of V-Sb-W-bearing rutile from the hemlo gold deposit, Ontario. *Can. Mineral.* 30, 319–326.
- Verberne, R., Reddy, S.M., Lantman, H.W.V.S., Alvaro, M., Wallis, D., Fougereuse, D., Langone, A., Rickard, W.D.A., 2022. Trace-element heterogeneity in rutile linked to dislocation structures: Implications for Zr-in-rutile geothermometry. *J. Metam. Geol.* 2022 (May), 1–22. <https://doi.org/10.1111/jmg.12686>.
- Vho, A., Rubatto, D., Lanari, P., Regis, D., 2020. The evolution of the Sesia Zone (Western Alps) from Carboniferous to cretaceous: insights from zircon and allanite geochronology. *Swiss J. Geosci.* 113, 24. <https://doi.org/10.1186/s00015-020-00372-4>.
- Warr, L.N., 2021. IMA–CNMNC approved mineral symbols. *Mineral. Mag.* 85, 291–320. <https://doi.org/10.1180/mgm.2021.43>.
- Xia, X., Ren, Z., Wei, G., Zhang, L., Sun, M., Wang, Y., 2013. In situ rutile U–Pb dating by laser ablation-MC-ICPMS. *Geochem. J.* 47, 459–468. <https://doi.org/10.2343/geochemj.2.0267>.
- Zack, T., Kooijman, E., 2017. Petrology and geochronology of rutile. *Petrochronol. Methods Appl.* 83, 443–467. <https://doi.org/10.2138/rmg.2017.83.14>.
- Zack, T., von Eynatten, H., Kronz, A., 2004a. Rutile geochemistry and its potential use in quantitative provenance studies. *Sediment. Geol.* 171, 37–58. <https://doi.org/10.1016/j.sedgeo.2004.05.009>.
- Zack, T., Moraes, R., Kronz, A., 2004b. Temperature dependence of Zr in rutile: Empirical calibration of a rutile thermometer. *Contrib. Mineral. Petrol.* 148, 471–488. <https://doi.org/10.1007/s00410-004-0617-8>.
- Zack, T., Stockli, D.F., Luvizotto, G.L., Barth, M.G., Belousova, E., Wolfe, M.R., Hinton, R. W., 2011. In situ U–Pb rutile dating by LA–ICP–MS: 208Pb correction and prospects for geological applications. *Contrib. Mineral. Petrol.* 162, 515–530. <https://doi.org/10.1007/s00410-011-0609-4>.
- Zhang, J., Jin, Z., Green, H.W., Jin, S., 2001. Hydroxyl in continental deep subduction zone: evidence from UHP eclogites of the Dabie mountains. *Chin. Sci. Bull.* 46, 592–596. <https://doi.org/10.1007/BF02900418>.